

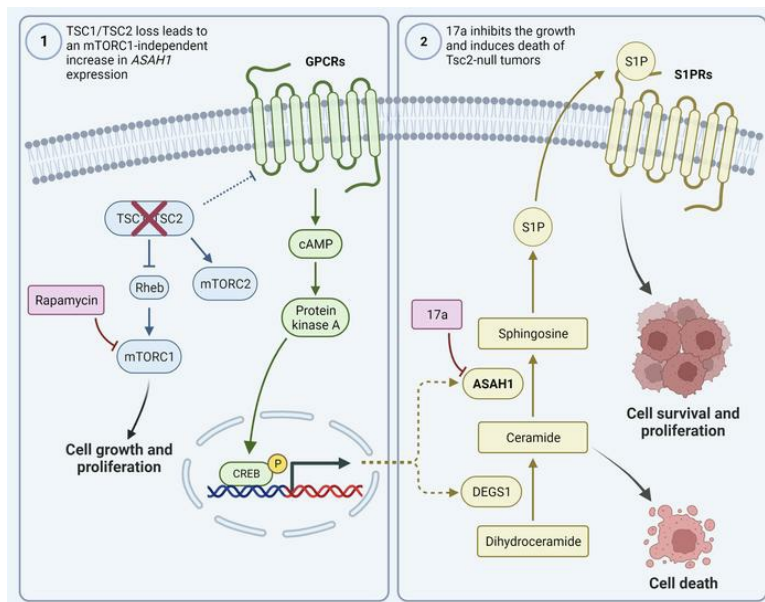
Upregulation of acid ceramidase contributes to tumor progression in Tuberous Sclerosis Complex

Aristotelis Astrinidis, ... , Yan Xu, Jane Yu

JCI Insight. 2023. <https://doi.org/10.1172/jci.insight.166850>.

Research In-Press Preview Cell biology Metabolism

Graphical abstract



Find the latest version:

<https://jci.me/166850/pdf>



Upregulation of acid ceramidase contributes to tumor progression in Tuberous Sclerosis

Complex

Aristotelis Astrinidis^{1*}, Chenggang Li^{1*}, Erik Y. Zhang^{1*}, Xueheng Zhao^{2,3}, Shuyang Zhao⁴, Minzhe Guo^{3,4}, Tasnim Olatoke¹, Ushodaya Mattam¹, Rong Huang², Alan G. Zhang¹, Lori Pitstick¹, Elizabeth J. Kopras¹, Nishant Gupta¹, Roman Jandarov⁵, Eric P. Smith¹, Elizabeth Fugate⁶, Diana Lindquist⁶, Maciej M. Markiewski⁷, Magdalena Karbowniczek⁷, Kathryn A. Wikenheiser-Brokamp^{8,9}, Kenneth D. R. Setchell^{2,3}, Francis X. McCormack¹, Yan Xu^{3,4}, and Jane J. Yu¹

¹ Department of Internal Medicine, University of Cincinnati College of Medicine, Cincinnati, Ohio, USA

² Clinical Mass Spectrometry Laboratory, Division of Pathology and Laboratory Medicine, Cincinnati Children's Hospital Medical Center, Cincinnati, Ohio, USA

³ Department of Pediatrics, University of Cincinnati College of Medicine, Cincinnati, Ohio, USA

⁴ Divisions of Pulmonary Biology and Biomedical Informatics, Perinatal Institute, Cincinnati Children's Hospital Medical Center, Cincinnati, Ohio, USA

⁵ Department of Environmental and Public Health Sciences, University of Cincinnati College of Medicine, Cincinnati, Ohio, USA

⁶ Department of Radiology, Cincinnati Children's Hospital Medical Center, Cincinnati, Ohio, USA

⁷ Department of Immunotherapeutics and Biotechnology, Jerry H. Hodge School of Pharmacy, Texas Tech University Health Sciences Center, Abilene, Texas, USA

⁸ Division of Pathology and Laboratory Medicine, Division of Pulmonary Medicine, and The Perinatal Institute Division of Pulmonary Biology, Cincinnati Children's Hospital Medical Center, Cincinnati, Ohio, USA

⁹ Department of Pathology and Laboratory Medicine, University of Cincinnati College of Medicine, Cincinnati, Ohio, USA

Corresponding Author: Jane J. Yu, Division of Pulmonary, Critical Care, and Sleep Medicine, Department of Internal Medicine, University of Cincinnati College of Medicine, 231 Albert Sabin Way, Cincinnati, OH, 45267, USA, Tel. +1-513-558-4114, yuj9@ucmail.uc.edu

Equal contribution statement: AA, CL and EYZ share first authorship. The order of co-first authors was determined based on intellectual contribution and volume of work.

Conflict-of-interest Statement: The authors have declared that no conflict of interest exists.

Running title: Dysregulation of sphingosine signaling in TSC

Key words: tuberin; TSC2; acid ceramidase; ASAH1; sphingolipid biosynthesis; tumorigenesis; single-cell RNA sequencing; scRNA-seq; mTOR inhibitor; rapamycin; sirolimus; tuberous sclerosis complex; lymphangioliomyomatosis

Abstract

Tuberous Sclerosis Complex (TSC) is characterized by multi-system low-grade neoplasia involving the lung, kidneys, brain, and heart. Lymphangi leiomyomatosis (LAM) is a progressive pulmonary disease affecting almost exclusively women. TSC and LAM are both caused by mutations in *TSC1* and *TSC2* that results in mTORC1 hyperactivation. Here, we report that single-cell RNA sequencing of LAM lungs identified activation of genes in the sphingolipid biosynthesis pathway. Accordingly, the expression of acid ceramidase (*ASAH1*) and dihydroceramide desaturase (*DEGS1*), key enzymes controlling sphingolipid and ceramide metabolism, was significantly increased in *TSC2*-null cells. *TSC2* negatively regulated the biosynthesis of tumorigenic sphingolipids, and suppression of *ASAH1* by shRNA or the inhibitor ARN14976 (17a) resulted in markedly decreased *TSC2*-null cell viability. *In vivo*, 17a significantly decreased the growth of *TSC2*-null cell derived mouse xenografts and short-term lung colonization by *TSC2*-null cells. Combined rapamycin and 17a treatment synergistically inhibited renal cystadenoma growth in *Tsc2*^{+/-} mice, consistent with increased *ASAH1* expression and activity being rapamycin insensitive. Collectively, the present study identifies rapamycin-insensitive *ASAH1* upregulation in *TSC2*-null cells and tumors and provides evidence that targeting aberrant sphingolipid biosynthesis pathways has potential therapeutic value in mTORC1-hyperactive neoplasms including TSC and LAM.

Summary

This study identifies rapamycin-insensitive *ASAH1* upregulation in *TSC2*-null tumors and provides evidence that targeting aberrant sphingolipid biosynthesis pathway has potential therapeutic value in TSC/LAM and neoplasms.

Introduction

Tuberous Sclerosis Complex (TSC) is an autosomal dominant disorder with multi-system manifestations, including low-grade neoplasms in the brain, heart, lungs, and kidneys (1-3).

Complications associated with TSC tumors include cognitive impairment, intractable seizures, autism, and renal hemorrhage and insufficiency. Lymphangiomyomatosis (LAM) is another TSC deficiency disorder resulting in progressive lung disease affecting almost exclusively women (4). LAM presents with fatigue, dyspnea, pneumothorax, and progressive loss of pulmonary function.

Approximately 50% of adult women with TSC and 10% of men with TSC have cystic changes on chest radiology consistent with LAM (5-8). TSC and LAM are caused by inactivating mutations in *TSC1* or *TSC2* (9-11), which encode hamartin and tuberin, respectively. Hamartin and tuberin form a complex with GTPase activating protein activity toward Ras homolog enriched in brain (Rheb), an activator of the mechanistic target of rapamycin complex 1 (mTORC1) (12-14). Thus, loss-of-function mutations in either *TSC1* or *TSC2* result in constitutive activation of mTORC1. mTOR is a serine/threonine protein kinase that functions as the catalytic subunit in two complexes, mTORC1 and mTORC2 (15). mTORC1 contains Raptor and phosphorylates several substrates, including ribosomal protein S6 kinase (S6K1/2), translational repressor 4E-binding protein 1 (4E-BP1) and ULK1, thereby regulating ribosome biogenesis, mRNA translation, protein synthesis, autophagy, cell metabolism, gene transcription, and cell growth (16-18). mTORC2 contains Rictor and phosphorylates protein kinases, including PKC and AKT at Serine 473, to control cell survival, cytoskeletal organization, and cell motility (19).

The discovery that *TSC1* or *TSC2* mutations cause dysregulation of mTORC1/mTORC2 led to preclinical studies (20-25) and human clinical trials demonstrating therapeutic efficacy of mTORC1 inhibitors in TSC and LAM (26-31). However, the use of mTORC1 inhibitors (mTORi) in LAM and TSC has several limitations, including: 1) the effect on tumor growth is cytostatic rather than cytotoxic, 2) tumors typically regrow upon treatment cessation (26, 28, 32-34), 3) some mTOR related disease

manifestations are poorly responsive to therapy, and 4) patients are at significant risk for potential side effects given the need for long-term treatment. Thus, there is a need to optimize mTORi approaches and to develop novel remission inducing therapies.

We previously reported that prostaglandin biosynthesis and functions are dysregulated in TSC2-deficient cells (35-38). Prostaglandin E2 receptors (EP1-4) are G protein-coupled receptors that integrate signals to regulate various cellular functions (39, 40), including cyclic AMP production and transactivation of gene expression, including *ASAH1* (41). We found that TSC2-null angiomyolipoma (AML)-derived cells produce excessive PGE₂ induced by COX2 and express higher levels of PGE₂ receptor 3 (EP3) relative to TSC2-reexpressing cells (35-38). These results suggest an interplay between PGE₂ activity and sphingolipid metabolism in TSC-deficient tumors. Sphingolipids are major components of the eukaryotic plasma membrane that mediate multiple essential cellular functions, including apoptosis, proliferation, stress responses, necrosis, inflammation, autophagy, senescence, tumor growth (42, 43), cancer progression, and differentiation (43). Ceramide and sphingosine-1-phosphate (S1P), the two central bioactive sphingolipids, exhibit opposing roles in regulating cancer cell death and survival (43-45). Ceramide is considered to be at the core of sphingolipid metabolism and intracellular concentrations of this intermediary directly increase apoptosis and cell cycle arrest (46). The rate limiting step of *de novo* ceramide synthesis is the condensation of palmitate and serine by serine palmitoyl transferase. The final reaction to produce ceramide from dihydroceramide is catalyzed by delta 4-desaturase sphingolipid 1 (dihydroceramide desaturase, DEGS1). N-acylsphingosine amidohydrolase 1 (acid ceramidase, *ASAH1*) catalyzes the cleavage of ceramide to sphingosine and fatty acids, and controls the sphingosine/ceramide ratio (43, 46). Carmofur, a derivative of 5-fluorouracil, is a broad-spectrum antimetabolite that impacts a wide range of pathways. Studies of carmofur activity in colorectal cancer cells (47), colorectal carcinoma patients (48), glioblastoma cells (49), and breast cancer cells (50) demonstrate that carmofur is effective in suppressing *ASAH1* expression.

Here, we report the identification of sphingolipid biosynthesis pathway genes in disease-defining LAM lung cells by single-cell RNA-sequencing. Analysis of publicly available expression array data from TSC2-null AML-derived cells (51) revealed that *DEGS1* and *ASAH1* transcripts were significantly increased in TSC2-null AML-derived cells, compared to TSC2-reexpressing cells. Moreover, we discovered TSC2 dependent upregulation of *DEGS1* and *ASAH1* expression in cell models of human angiomyolipoma-derived cells and in clinical renal AMLs and pulmonary LAM patient specimens. Mechanistic studies showed that enhanced expression of *DEGS1* and *ASAH1* is independent of mTORC1 inhibition, which is novel and previously unexplored. Together, our studies identify rapamycin-insensitive upregulation of enzymes contributing to sphingolipid metabolism in TSC2-null cells and tumors. Our studies reveal a novel function of TSC2 that negatively regulates sphingolipid production and action via *ASAH1*. Thus, targeting aberrant sphingolipid biosynthesis pathways has potential therapeutic value in TSC and LAM patients as well as possibly in other mTORC1-hyperactive neoplasms.

Results

Single-cell RNA-sequencing identifies sphingolipid biosynthesis pathway gene activation in disease-defining LAM lung lesion cells. We previously employed single-cell RNA-sequencing (scRNA-seq) and systems biology tools to identify LAM cells, define their signature genes and enriched functions, and delineate altered signaling pathways associated with LAM pathogenesis (52). In the present study, we integrated scRNA-seq of LAM lungs (n=2, GSE135851) and control female lung samples (n=6, GSE122960) resulting in a total of 54,511 cells that were clustered into distinct cell lineages based on expression of lineage specific markers (Epithelium: EPCAM, CDH1; Endothelium: CDH5, EMCN; Mesenchymal: TCF21, ACTA2; Immune: PTPRC, CD68) (**Fig. 1A**). Differentially expressed genes were identified by comparing 190 mesenchymal cells from LAM lung samples with 736 mesenchymal cells from control samples (**Fig. 1B**) and subject to gene set enrichment analysis. Gene set enrichment analysis of genes included in LAM lung cells revealed significant enrichment of “sphingolipid metabolic process”, “glycosphingolipid catabolic process” and “response to cAMP” in LAM vs control (**Fig. 1C**). Among these genes, *ASAH1* and *DEGS1* mRNA expression levels and frequency of *ASAH1* and *DEGS1* positive cells within the LAM mesenchymal clusters were significantly increased relative to control mesenchymal cells (**Fig. 1D-1E**). In addition, we analyzed scRNA-seq data from one renal AML harboring a *TSC1* mutation (52). Visualization of 1,583 cells from the AML lesion showed three major cell types: ACTA2+ AML cells (Cluster 1), endothelial cells (Cluster 2) and immune cells (Cluster 3) (**Fig. 1F**). A dot plot revealed abundant expression of selected sphingolipid pathway genes *ASAH1*, *DEGS1*, *SPHK1* and *SPHK2* in ACTA2+ AML cells (**Fig. 1G**). Feature plots of ACTA2+ AML cells showed selective expression of known LAM and AML markers, including *ACTA2*, *PMEL*, *FIGF*, and *CTSK*, and several key sphingolipid pathway genes, including *ASAH1*, *DEGS1*, *SPHK1*, and *SPHK2*, were selectively expressed in the same ACTA2+ AML cell cluster (**Fig. 1H**). Collectively, our scRNA-seq analysis identified selective

activation of *ASAH1* and *DEGS1* genes in LAM lung and renal AML cells that are worth further investigation.

Differential expression of acid ceramidase *ASAH1* is evident in lymphangiomyomatosis lesions. Activation of the sphingolipid biosynthesis pathway leads to sphingosine production and bioactive lipid signaling molecule activation, which positively impacts cell viability and tumor progression (43, 46). Note that AMLs have “mesenchymal” characteristics, containing immature smooth muscle cells, adipose cells, and aberrant blood vessels (53). To determine whether the sphingolipid biosynthesis pathway (**Fig. 2A**) is activated in LAM, we compared gene expression data from non-LAM female lungs (n=15) to LAM lungs (n=14) and found that *ASAH1* and *DEGS1* transcript levels were significantly higher in LAM (**Fig. 2B, 2C; Suppl. Fig. S1; and Suppl. Table T1; P<0.0001** Mann-Whitney test). To determine the protein levels of *ASAH1* in human lung lesions we performed immunohistochemical staining in LAM lung tissues obtained from the National Disease Research Exchange (NDRI). *ASAH1* protein colocalized with smooth muscle actin positive and phospho-S6 positive cells within LAM lung lesions, with *ASAH1* being upregulated in LAM lesions, compared to adjacent normal tissue (**Fig. 2D**). Immunoblot analysis showed a 4-fold increase in *ASAH1*/β-actin in the LAM lung tissue lysates, compared to normal lung (**Fig. 2E, 2F; Suppl. Fig. S2, and Suppl. Table S1, S2; unpaired t test P < 0.05**). Since *ASAH1* expression is regulated by cAMP-responsive element binding protein (CREB) (54), we tested CREB activation by immunoblotting with a phospho-CREB [Ser133] antibody demonstrating a 2.5-fold increase in p-CREB/CREB ratio (**Fig. 2E, 2F; Suppl. Fig. S2, and Suppl. Table S1, S2; unpaired t test P < 0.05**). Finally, we assessed *DEGS1* and *ASAH1* proteins in renal AML and normal kidney. *ASAH1* expression was evident in ACTA2-positive renal AML cells (brown staining). Stroma (thin red arrows) and infiltrating mononuclear cells (thin yellow arrows) were negative (**Fig. 2G**). We also found that both *ASAH1* and *DEGS1* colocalized with ACTA2- and phospho-S6-positive cells (**Fig. 2G**). *DEGS1* accumulation was present in a subpopulation of ACTA2-positive renal AML cells. Normal glomeruli (red arrowheads) and tubular

epithelial cells (black arrows) in the normal kidney lacked specific expression of ACTA2 and phospho-S6. Minimal DEGS1 staining was present in glomerular and tubular epithelial cells (**Fig. 2G**). Normal glomeruli contain abundance of mesenchymal origin mesangial cells that provide support for glomerulus capillary network (55). Therefore, our controls contain epithelial and mesenchymal components of normal kidney, and expression of ASAH1 and DEGS1 was evaluated in both components. ASAH1 staining was negative in glomeruli, whereas some epithelial tubular cells express low levels of ASAH1. DEGS1 seems to be expressed in some glomerular and tubular cells (**Fig. 2G**). Collectively, these data provide evidence that the sphingolipid biosynthesis pathway proteins are evident in TSC2-null cells as well as LAM lung and kidney AML lesions.

TSC2 negatively regulates ASAH1 expression. To determine whether sphingolipid biosynthesis pathway gene expression is regulated by TSC2, we re-analyzed previously published genomic data from TSC2-null AML-derived cells (621-102) (51) and found that genes participating in the sphingolipid pathway were upregulated in TSC2-null cells (**Fig. 3A**) including *ASAH1*, *DEGS1* and *SPHK1* transcripts, compared to TSC2-addback 621-103 cells (**Fig. 3B**, **Suppl. Fig. S3**, and **Suppl. Table S1, S3**; *ASAH1* $P < 0.0001$, *DEGS1* $P < 0.0001$, and *SPHK1* $P = 0.0034$ by unpaired t test). Immunoblotting analysis showed that DEGS1 and ASAH1 proteins were also more abundant in TSC2-null 621-101 relative to TSC2-addback 621-103 cells, both in regular (10% FBS) and serum-free (0% FBS) culture conditions (**Fig. 3C, 3D**, **Suppl. Fig. S3**, and **Suppl. Table S1, S4**). These findings indicate aberrant upregulation of the sphingolipid biosynthesis pathway in TSC2-null AML-derived cells.

Cellular levels of sphingosine are elevated in a rapamycin-insensitive manner in LAM-derived cells. ASAH1 catalyzes the cleavage of ceramide to sphingosine. To determine whether the elevated ASAH1 expression in TSC2-null cells correlates with its enzymatic activity, we measured cellular levels of ceramides and sphingosine using LC-MS/MS. In TSC2-null cells the levels of ceramide were

three-fold lower (**Fig. 4A**), and the levels of sphingosine were two-fold higher (**Fig. 4B**), compared to TSC2-addback cells. Importantly, rapamycin treatment did not alter the levels of ceramides or sphingosine in TSC2-null cells, suggesting a rapamycin-insensitive regulation of ceramide conversion to sphingosine. Moreover, qRT-PCR analysis showed that *ASAH1* mRNA levels were 2.4-fold higher in TSC2-null cells, compared to TSC2-addback cells, and rapamycin did not affect *ASAH1* mRNA levels (**Fig. 4C**). Furthermore, *ASAH1* protein levels were higher in TSC2-null cells, compared to TSC2-addback cells, and rapamycin did not alter *ASAH1* protein levels while suppressing S6 phosphorylation as expected (**Fig. 4D**). We next treated TSC2-null cells with rapalink-1 (RLK1, 5 nM), a third generation mTORi that is a more potent mTORC1 inhibitor than rapamycin and other first- and second-generation mTORis. Although RLK1 treatment drastically suppressed phosphorylation of S6 and 4E-BP1, *ASAH1* protein levels were not affected (**Fig. 4E**). Collectively, our data indicate an mTOR-independent regulation of *ASAH1* expression and sphingolipid biosynthesis in TSC2-null cells.

ASAH1 expression is dependent on CREB and ERK activity. cAMP inhibits mTORC1 signaling in a TSC1/TSC2-independent manner (56). cAMP response element-binding protein (CREB) is tightly regulated by intracellular cAMP levels. Since we observed an upregulation of CREB phosphorylation in LAM lung tissue lysates (Fig. 2E, 2F), we assessed the cAMP levels in TSC2-null 621-101 and TSC2-reexpressing 621-103 cells and found that expression of TSC2 decreased intracellular cAMP levels by 3-4-fold (**Fig. 4F**). Consistent with these observations, TSC2-null cells had increased nuclear phospho-CREB [Ser133], compared to TSC2-reexpressing cells, which showed a diffuse cytoplasmic staining (**Fig. 4G**). To test whether increased CREB activation correlates with *ASAH1* expression, we treated TSC2-null cells with forskolin, an adenylyl cyclase activator that increases intracellular cAMP. *ASAH1* protein levels were increased in a dose-dependent manner (**Fig. 4H**). As expected, CREB phosphorylation was also increased by forskolin. Since activation of various pathways, including MAPK, Protein Kinase A (PKA), prostaglandins, and estrogen (57), increases phosphorylation of CREB, we tested whether perturbations of these pathways lead to alterations in

ASAH1 levels in TSC2-null cells. Inhibition of either MEK1/2, prostaglandin E2 receptor 3 (EP3), or PKA correlated with a significant decrease of ASAH1 protein levels (**Fig. 4I** and **4J**) and, with the exception of MEK1/2 inhibition, with a decrease in CREB phosphorylation (**Fig. 4I**). Finally, estradiol (E2) led to a 2-fold increase in *ASAH1* transcript levels (**Fig. 4K**) and immediate phosphorylation of CREB within 15 minutes (**Fig. 4I**), and a 2.7-fold increase in ASAH1 protein levels that was concomitant with a 2.8-fold increase in ER α within 24 hours (**Fig. 4M** and **4N**). Collectively, these data suggest that ASAH1 transcription and protein levels are dependent on CREB transcriptional activity.

ASAH1 inhibitors selectively reduce the viability of TSC2-null cells. To determine the effect of ASAH1 blockade on cell viability, we treated TSC2-null 621-101 cells with the ASAH1 inhibitor 17a (58), which selectively decreased the viability of TSC2-null cells in a dose-dependent manner with an IC₅₀=117 nM (**Fig. 5A**), but not of TSC2-addback 621-103 cells (IC₅₀=2,560 nM). Carmofur, a potent ASAH1 inhibitor that has been used to treat colorectal cancer patients in some countries (47, 59), selectively reduced the viability of TSC2-null cells in a dose-dependent manner (**Fig. 5B**, IC₅₀=17 μ M), and to a lesser extent TSC2-addback cells (IC₅₀= 253 μ M). These data support an important role for ASAH1 in enhancing TSC tumor cell viability.

Molecular depletion of ASAH1 inhibits the growth and induces apoptosis in AML-derived cells.

To determine whether ASAH1 is a key mediator of TSC2-null cell growth, we depleted *ASAH1* using siRNA. 621-101 cells transfected with *ASAH1* siRNA had 86.4% reduction of *ASAH1* transcript levels measured by qRT-PCR (**Fig. 5C**) and marked reduction of ASAH1 protein levels by immunoblotting (**Fig. 5D**). ASAH1 knockdown cells exhibited a 42% reduction in cell viability, compared to control siRNA treated cells (**Fig. 5E**), supporting a critical role for ASAH1 in TSC2-null cell viability. More importantly, *ASAH1* siRNA-transfected cells showed a significant increase in apoptosis, compared to control siRNA transfected cells (**Fig. 5F** and **5G**), which was further increased by ceramide treatment. Finally, we transduced TSC2-null AML-derived 621-101 cells with *ASAH1* shRNA lentiviruses or the

pLKO.1 control vector (**Fig. 5H**). Consistent with our previous results, *ASAH1* silencing resulted in significant reduction of cell viability (**Fig. 5I**) and a significant increase in apoptosis, compared to pLKO.1-transduced cells (**Fig. 5J-5L**). Collectively, these data support an important role for *ASAH1* in TSC2-null cell survival.

Suppression of *ASAH1* attenuates the progression of xenograft tumors of TSC2-null cells. We next assessed the possible benefit of the *ASAH1* inhibitor 17a in a xenograft tumor model in which Tsc2-null ELT3 luciferase-expressing cells were implanted subcutaneously into immunodeficient NOD *scid gamma*-null mice (25). Upon tumor development, mice were treated with 17a or vehicle control for four weeks. Bioluminescence imaging was performed weekly. 17a treatment decreased the bioluminescence intensity (**Fig. 6A**) and significantly reduced tumor growth by 2.7-fold, relative to vehicle control (**Fig. 6B**). To further assess the role of *ASAH1* in tumor growth, LAM AML-derived TSC2-null 621-101 cells expressing luciferase were transfected with shRNA-*ASAH1* (**Fig. 6C**) and inoculated in immunodeficient NOD *scid gamma* (NSG) mice. Bioluminescence signal was detectable at 21 weeks post-inoculation (**Fig. 6D**), and tumor growth was monitored until week 32 (**Fig. 6E**). *ASAH1* depletion significantly delayed the onset of tumors and decreased tumor progression by 4.2-fold, compared to pLKO.1 control transduced cells (**Fig. 6E and 6F**).

Finally, we assessed whether suppression of *ASAH1* affects the ability of TSC2-null cells to colonize the lungs in a mouse model we previously reported (25). Female NSG mice were pre-treated with 17a or vehicle for 48 hours prior to intravenous injection of luciferase-expressing 621-101 cells, and bioluminescence imaging in the thoracic region was used to quantify lung colonization at baseline, and at 6- and 24-hours post-injection (**Fig. 6G**). *ASAH1* blockade by 17a significantly reduced lung colonization of 621-101 cells at both timepoints (**Fig. 6H**). Similarly, we inoculated NSG mice with the same number of 621-101 luciferase-expressing cells transduced with pLKO.1 control shRNA or with two *ASAH1* shRNAs, and performed bioluminescence imaging at baseline and 6 and 24 hours post

inoculation (**Fig. 6I**). At both timepoints, both ASA1 shRNA-621-101 cells exhibited significantly decreased lung colonization, compared to pLKO.1 shRNA control cells (**Fig. 6J**). Collectively, these data support the notion that ASA1 contributes to TSC tumor progression and dissemination to the lungs in LAM. We postulate that combinatorial suppression of mTORC1 and ASA1 will inhibit tumor growth beyond what is achieved with mTORi alone.

Combination of acid ceramidase 1 inhibitor 17a and rapamycin suppresses development and progression of renal cystadenomas in Tsc2 heterozygous mice. Next, we tested this combination approach in Tsc2 heterozygous mice that develop spontaneously arising renal cystadenomas. The number of macroscopic renal lesions at week 12 was markedly decreased in mice treated with 17a or rapamycin. Importantly, the combinatorial treatment of 17a and rapamycin reduced the number of renal cystadenomas to a level that was better than that achieved by either agent alone (**Fig. 7A and 7B**).

To assess the efficacy of single or combinatorial treatment on tumor rebound after drug withdrawal, all treatments were discontinued at week 12 of drug administration. Renal cystadenoma progression was monitored by MRI at four- and eight-weeks after drug cessation (**Fig. 7C**). MRI imaging and quantification of individual cyst volume showed that cysts regrew within eight weeks after withdrawal of rapamycin treatment. In contrast, renal cysts in mice withdrawn from the combinatorial treatment did not regrow, although those withdrawn from 17a treatment exhibited moderate regrowth (**Fig. 7D and 7E**). Moreover, at the end of the drug withdrawal study at 4-week and 8-week observation phases, renal lesions were counted under dissecting microscope (60). Four weeks post drug discontinuation the number of macroscopic renal cysts were significantly lower in mice withdrawn from rapamycin or rapamycin plus 17a treatments relative to that in mice withdrawn from 17a treatment (**Fig. 7F**). Importantly, the combinatorial treatment of rapamycin and 17a significantly suppressed the regrowth of renal cystadenomas at the end of 8-weeks observation period, compared

to either agent alone (**Fig. 7F**). Collectively, our data provide evidence that the combinatorial inhibition of mTORC1 and ASAH1 suppresses the progression and regrowth of renal cystadenomas after drug cessation *in vivo*.

To assess the mechanisms for 17a-dependent delay in post-treatment regrowth of renal cysts/cystadenomas, we performed immunohistochemical staining of phospho-S6 [Ser235/236] and proliferating cell nuclear antigen (PCNA), as well as TUNEL assay in kidneys from mice withdrawn from treatments. We found that cells lining renal cysts and in renal lesions were positive for phospho-S6 (**Fig. 7G**), indicative of mTORC1 hyperactivation. TUNEL staining was negative in kidneys from mice in all groups (**Fig. 7G**), suggesting either that treatments did not induce apoptosis in cystadenoma lesions or that apoptotic cystadenoma cells were rapidly cleared after drug withdrawal. Quantification of PCNA immunoreactivity in tumors after drug withdrawal showed a significant reduction in PCNA nuclear positivity for the 17a alone and rapamycin + 17a combinatorial treatment groups, compared to vehicle- and rapamycin-only treatment groups (**Fig. 7G** and **7H**). These data suggest that the 17a-dependent delay in post-treatment regrowth is due to a reduction in Tsc2-null tumor cell proliferation.

Discussion

Sphingolipids play critical roles in kidney physiology (61), chronic inflammation, and cancer progression (39, 40). Various sphingolipids have widely differing cellular actions and we postulated that they may impact renal AML-derived cell viability. In this study, we show that the increased growth of TSC and LAM tumors are, at least in part, attributed to the aberrant expression of DEGS1 and ASAH1 resultant changes in sphingolipid levels. We found that renal AMLs accumulate abundant levels of DEGS1 and ASAH1 and that ASAH1 suppression leads to reduced viability and increased apoptosis of TSC2-null cells. Furthermore, TSC2 negatively regulates ASAH1 expression and sphingosine production in an mTOR inhibitor-independent manner.

Our data show that rapamycin suppresses mTORC1 activation, as assessed by phospho-S6 levels, but has no effect on ASAH1 expression or activity in TSC2-null cells. There are several potential explanations for this finding. Studies by Choo et al. have shown that rapamycin's inhibition of mTORC1 is incomplete (62) and mTORC2 dysfunction has been observed in TSC2-null cells (63). There is further evidence that TSC2 may have other functions in addition to inhibiting mTORC1 or mTORC2. Here we sought to determine the mechanism by which TSC2 regulates the expression of sphingolipid biosynthesis genes and found that cAMP-CREB mediates the ASAH1 expression in TSC2-null cells.

It is important to note that mTORi act principally on mTORC1 rather than mTORC2, even though TSC mutations affect both complexes. Logically, the mTORC2-mediated pathways likely contribute to mTORC1 independent cellular behaviors in the presence of TSC mutations or mTORi treatment (3). Notably, B-Raf kinase activity is reduced in TSC2-null cells due to an mTORC1-independent action of Rheb (64, 65). *Tsc1*^{-/-} and *Tsc2*^{-/-} mouse embryonic fibroblasts (MEFs) have a higher percentage of ciliated cells compared to controls and the mTORi rapamycin has no effect on the abundance of cilia

(66). A recent study suggests that sphingolipid metabolism, a well-known target of mTORC2-mediated pathways, may be of importance (67).

We, and others, have previously shown that estrogen promotes MAPK phosphorylation in TSC2-null cells *in vitro* (25, 35, 68-71) and *in vivo* (25). We also reported that estrogen increased prostaglandin biosynthesis (35) and functions via prostaglandin receptor EP3 (36). In the present study, we found TSC2-null cells exhibited higher cellular levels of cAMP, phosphorylation of CREB, and nuclear localization of phospho-CREB (Fig. 4F, G), indicating the activation of cAMP-CREB. We also found that E2 treatment increased the transcript and protein levels of ASAH1 in TSC2-null cells (Fig. 4K, L). Importantly, elevated protein levels of ASAH1 were attenuated by a MEK-MAPK inhibitor (AZD6244), an EP3 antagonist (L798106), and a PKA inhibitor (PKI) (Fig. 4I), suggesting the action of MAPK and PKA in enhancing ASAH1 expression in TSC2-null cells. It has been reported that CREB is a transcription factor mediating ASAH1 expression in human adrenocortical cells (54). PKA and MAPK also activate CREB (57). Thus, our current study reveals a connection between estrogen, MAPK, prostaglandin action, cAMP-CREB, and ASAH1 expression in TSC2-null cells, consistent with other reported findings.

Renal AMLs are a major clinical manifestation of TSC. These tumors are composed of aberrant blood vessels, smooth muscle cells, and adipose cells (53). We found increased DEGS1 and ASAH1 protein levels in renal AML cells from three patients. We have shown that TSC renal AMLs express abundant DEGS1 and ASAH1 proteins relative to adjacent normal kidney tissues. Treatment with rapamycin alone has a cytostatic rather than remission-inducing effect in clinical trials and in preclinical models of TSC. These data suggest that, within the context of mTORC1 inhibitor actions, there are primary pathways provoked by TSC mutations that promote persistent proliferative states. Our studies show that suppression of ASAH1 using 17a and ASAH1-shRNA attenuates xenograft tumor progression and growth of renal cystadenomas in *Tsc2^{+/-}* AJ mice. Our data supports the

concept that the selectively increased expression of DEGS1 and ASAH1 in TSC tumor cells leads to increased sphingolipid biosynthesis, which in turn enhances TSC tumor cell viability and growth in preclinical models. Interestingly, studies have shown that *Tsc2*^{-/-} MEFs are resistant to ceramide-triggered death (72). Collectively, these results suggest a cell context-specific regulation of sphingolipid metabolism and actions in TSC.

In summary, the present study identified increased expression of key enzymes in the sphingolipid biosynthesis pathway in LAM and AML tumor cells as well as in TSC2-null cells. The activation of sphingolipid biosynthesis pathway in TSC-deficient cells and tumors is rapamycin insensitive. We further showed that TSC2 regulates ASAH1 to increase sphingolipid production and activity. Thus, we have identified the sphingolipid biosynthesis pathway as a promising therapeutic target with potential clinical value in TSC and LAM, and possibly in other mTORC1-hyperactive neoplasms.

Methods

Single-cell RNA-sequencing analysis. LAM lung tissue collection, scRNA-seq data analyses, and cell type annotation were described in detail in Guo et al., 2020 (52). In the present study, we integrated scRNA-seq of LAM lungs (n=2, GSE135851), control female lung samples (n=6, GSE122960) and renal angiomyolipoma (AML) (n=1, GSE135851/GSM4035469). Cell type annotation is done based on the previous study (52)). For LAM lungs and control lungs, a total of 54,511 cells were clustered and dissected into major lineages based on lineage pan markers (epithelial: EPCAM, CDH1; endothelial: PECAM1, CDH5; mesenchymal: TCF21, ACTA2; immune: PTPRC, CD68). Differentiated expressed gene between LAM^{CORE} and control mesenchymal cells were identified using Wilcoxon signed rank test. Functional enrichment analysis was performed using ToppGene suite (73).

Cell culture and reagents. Eker rat uterine leiomyoma derived (ELT3) cells (74, 75) were kindly provided by Dr. C. Walker (Institute of Biosciences and Technology Texas A & M University, Houston, TX). ELT3 cells stably expressing luciferase (ERL4) and LAM patient-associated angiomyolipoma-derived (621-101) cells were kindly provided by Dr. E.P. Henske (Brigham and Women's Hospital-Harvard Medical School, Boston, MA) (25, 76). Cells were cultured in DMEM/F12 supplemented with 10% FBS, and 1% penicillin-streptomycin-amphotericin B (PSA).

Confocal Microscopy. ELT3 and LAM-derived cells were plated overnight on glass coverslips in 12-well tissue culture plates. Cells were serum starved overnight, and then treated with 20 nM rapamycin for 24 hrs. Cells were rinsed with PBS twice, fixed with 4% paraformaldehyde for 30 min at 37°C, permeabilized with 0.2% Triton X-100, blocked in 3% BSA/PBS for 1 hr, and then incubated with primary antibodies in 1% BSA/PBS for 1 hr followed by secondary antibodies for 1 hr at room temperature. Images were captured with a FluoView FV-10i Olympus Laser Point Scanning Confocal Microscope.

Expression array analysis. Re-analysis of previously published expression array data (GEO accession number GSE16944) (51) was performed using GEO2R online tool. Transcript levels were compared between TSC2-deficient (TSC2-) and TSC2-addback (TSC2+) cells, or rapamycin-treated and vehicle-treated TSC2-deficient (TSC2-) cells.

siRNA transfections. Two separate human *ASAH1*-siRNAs (50 nM) (Dharmacon) were transfected into 621-101 cells using Lipofectamine RNAiMAX (Invitrogen) according to the manufacturer's protocols. Cells were harvested 48 hours post-transfection.

shRNA downregulation. HEK-293T packaging cells were transfected with *ASAH1* shRNA, or non-Targeting shRNA vectors using Trans-IT TKO Transfection reagent (Mirus). 621-101 cells were transduced with lentiviruses for 48 hr and then selected with puromycin. Stable clones were harvested for future experiments.

Quantitative RT-PCR. RNA from cultured cells was isolated using RNeasy Mini Kit (Qiagen). Gene expression was quantified using One-Step qRT-PCR Kits (Invitrogen) in the Applied Biosystems Step One Plus Real-Time PCR System and normalized to *ACTB* (human β -actin) or *Tuba1a* (rat α -tubulin). PCR Primers sequences are: *ASAH1* forward 5'-CTTTGCTGGCTATGTGGGCATG-3' and reverse 5'-TGAGGAACCCTATCCACATGGC-3', and *ACTB* forward 5'-AGAGCCTCGCCTTTGCCG-3' and reverse 5'-CCCACGATGGAGGGGAAGAC-3'.

Immunofluorescence staining. Sections were deparaffinized, incubated with primary antibody (1:100 in PBS+3%BSA) and smooth muscle actin (SMA, 1:200 in PBS+3% BSA, Santa Cruz, #sc32251), and secondary antibodies (1:1,000, Invitrogen, #A-21202 and #A10042). Images were captured with Fluorescence Microscope (Olympus BX60).

Fluorescence-activated cell sorting. 621-101 cells were stained with Annexin V-FITC Apoptosis Detection Kit I (BD #556547) according to the manufacturer's protocols. FACS analysis was carried out on BD FACSCanto™ II.

LC/MS-MS profiling of sphingolipids. Acetonitrile, methanol, isopropanol, ethyl acetate, and formic acid (99%) were purchased from Fisher Science (Waltham, MA). Ammonium formate was analytical grade and purchased from Sigma-Aldrich (St Louis, MO). Sphingosine (d17:1), ceramide (d18:1/17:0), sphingosine (d18:1), ceramide (d18:1/16:0), ceramide (d18:1/18:0), ceramide (d18:1/24:0) were purchased from Avanti Polar Lipids (Alabaster, AL). Calibration standards containing 0, 0.1, 1, 5, 10, 20 ng/ml of sphingosine and 0, 10, 100, 500, 1000, 2000 ng/ml ceramides (including ceramide (d18:1/16:0), ceramide (d18:1/18:0), ceramide (d18:1/24:0)) are prepared by pipetting the appropriate volume of standards into the charcoal stripped human serum (Equitech-bio lab, Kerrville, TX). Calibrators were extracted using the same procedure as the plasma samples. Quantification of sphingolipid species was based on respective calibration curves from sphingosine and ceramides. Plasma samples were stored at -80°C and allowed to thaw at 4°C for 2 h. Extraction of sphingolipids from plasma samples (25 μl) was conducted with a modified method based on Hammad et al. (77). Briefly, D.I. water (950 μl) was first added to each sample, which was also fortified with 25 μl of appropriate internal standards (appropriate concentration of C17-sphingosine and C17-Ceramide in MeOH). The samples were then extracted with 1 ml extraction solution consisting of isopropanol and ethyl acetate (15:85 v/v). After centrifugation for 5 min at 4,000 rpm, the upper organic phase was collected. The remaining diluted plasma was then acidified with 50 μl formic acid (98%), and an additional 1 ml of extraction solution was added to further facilitate completion of extraction. The organic phase was then combined and was evaporated to dryness. The dried residues were reconstituted in 150 μl methanol and transferred to HPLC auto-sampler vials for UPLC-

MS/MS analysis. For ceramide analysis, extraction samples were further diluted 10 times with methanol due to their high concentrations. Quantification of sphingolipids was performed by a UHPLC system coupled to a triple-quadrupole mass spectrometry (Waters, Milford, MA). Multiple Reaction Monitoring (MRM) mode was used for quantification of sphingolipids and chromatography was conducted on an Acquity UHPLC BEH C18 column (2.1×100 mm, 1.7 μm, Waters, Milford, MA). The optimal signal for the ion pairs of sphingosine and ceramides was achieved in positive ion mode with the following instrument settings: capillary voltage, 2.0 kV; cone voltage 10 V; desolvation temperature, 400°C; desolvation gas flow, 900 L/h; and cone gas flow, 10 L/h. Helium was used as the collision gas. A gradient mobile phase was used with a binary solvent system, which ramped from 40% solvent B to 100% solvent B over 4 min, after which it was held for 5 min, then changed to 40% solvent B over 0.1 min before being held for 2.9 min for re-equilibration. The total run time was 10 min using a flow rate at 0.4 ml/min. Solvent A consisted of water/methanol (95/5 v/v) with 10 mM ammonium formate and 0.1% formic acid; solvent B consisted of methanol with 10 mM ammonium formate and 0.1% formic acid. Details of the MRM transitions monitored and the cone and collision voltages, and retention times for analytes and internal standards are shown in **Table 1** and **Table 2**. Data were acquired and processed with Masslynx 4.1 software (Waters).

Cell viability assay. Cell viability was estimated using the 3-(4,5-dimethylthiazol-2-yl)-2,5-diphenyl tetrazolium bromide (MTT) assay. TSC2-null 621-101 and TSC2-addback 621-103 cells were plated in 96 well plates (2×10^3 cells/well). Cells were incubated in 37°C CO₂ incubator for 24h before treatment with escalating concentrations of 17a (Cayman 17119) or Carmofur (Selleck S1289) for 72 h. 25 μl of MTT solution (2.5 mg/ml growth media) was added to each well, followed by 4 h incubation at 37°C. Formation of formazan crystals was observed under the microscope. At the end of treatment, an equal volume of 0.04 N HCl in isopropanol was added, followed by 1.5 h incubation of plates at

37°C. Absorbance at 560 nm was measured in a Synergy HTX multi-mode reader (Biotek) with a reference of 650 nm. GI₅₀ was calculated using CompuSyn software (ComboSyn, Inc) (78).

Immunohistochemistry. Sections were deparaffinized, incubated with primary antibodies and biotinylated secondary antibodies and counterstained with Gill's Hematoxylin. Cell death was assessed using TUNEL assay (Cell Signaling Technology, CST#48513).

Drug formulation for *in vivo* studies. Two hours prior to treatment, rapamycin (Enzo) was diluted in 10% PEG300, 0.5% Tween 80 in PBS (Corning). 17a (Cayman) was diluted in PBS (Corning).

Animal studies. For ELT3-based studies, female C.B-*Igh-1^b/IcrTac-Prkdc^{scid}* (SCID) mice at 4-6 week of age were purchased from Taconic Biosciences (Germantown, NY). For 621-101-based studies, female NOD.Cg-*Prkdc^{scid} Il2rg^{tm1Wjl}/SzJ* (NSG) mice at 7-8 weeks of age were purchased from The Jackson Laboratory. Animal health was monitored daily during studies. Animal weight was monitored weekly.

For xenograft studies, 2x10⁶ ELT3-luc or 10⁷ 621-101-luc cells were resuspended in PBS with 25% Matrigel (BD) and injected subcutaneously into the flanks of mice as previously described (25). Upon tumor onset, mice were randomized into two groups: vehicle and 17a (10 mg/kg/day, i.p.) (49). Treatments were given 5 times/week for four weeks (or less, if necessary, because of animal pain or distress).

For short-term lung colonization studies, NSG mice were pre-treated with vehicle or 17a (10 mg/kg/day, i.p.) for 2 days before cell inoculation. 2x10⁵ 621-101-luc cells were resuspended in 0.1 ml PBS and injected into mice intravenously as previously described (25).

For renal cystadenoma studies, *Tsc2*^{+/-} A/J mice at 9 months old were obtained as a generous gift from Dr. Steve Roberds (Tuberous Sclerosis Alliance, Washington, DC). *Tsc2*^{+/-} A/J mice develop renal cystadenomas at high frequencies (79, 80). Four treatment groups were studied, including one vehicle control group. Mice were treated at five months of age with rapamycin (3 mg/kg/day, i.p.), 17a (10 mg/kg/day, i.p.), and rapamycin plus 17a (3 mg/kg/day, i.p. + 10 mg/kg/day, i.p.). Treatments were given five times/week. Eight animals were treated for four months and then sacrificed at nine months of age. To examine tumor regrowth, eight mice were withdrawn from treatment for two months and then sacrificed at 11 months of age. Renal tumor burden was assessed by Magnetic Resonance Imaging (MRI) every 4 weeks.

Bioluminescent reporter imaging. Ten minutes before imaging, mice were given D-luciferin (120 mg/kg, i.p., PerkinElmer Inc., # 122799). Bioluminescent signals were recorded using the Xenogen IVIS Spectrum System. Total photon flux of chest regions was analyzed as previously described (25).

T2 weighted MRI to assess renal tumor progression in *Tsc2*^{+/-} mice. MRI scans were carried out by the In vivo Microimaging Laboratory at Cincinnati Children's Hospital Medical Center using a 9.4T vertical bore Bruker Biospec system using a 36 mm diameter volume transmit/receive coil (81). Mice were anesthetized with isoflurane and positioned in the center of the coil and magnet. Fat suppressed, respiratory triggered 2D fast spin echo data were acquired using a repetition time of 3400 ms, an echo time of 42 ms, 4 averages, an echo spacing of 14 ms with 8 echoes acquired per repetition time, a matrix of 256 x 256 with a 29.5 mm x 29.5 mm field-of-view with a 50 kHz bandwidth, 0.5 mm slice thickness and 19 slices to cover kidney.

Statistical analyses. Unless otherwise specified, data in graphs represent mean \pm SD. Statistical analyses and plotting were performed using GraphPad Prism version 9.5.1, including unpaired t test and Mann-Whitney test when comparing two groups for *in vitro* and *in vivo* studies, unpaired t test

with Bonferroni multiple comparison adjustments, and one- and two-way ANOVA tests for multiple group comparison (Dunnett's multiple comparisons test when comparing multiple groups with control group, Tukey's multiple comparisons test when making multiple pair-wise comparisons between different groups). A P value less than 0.05 was considered significant.

Study approval. The University of Cincinnati Standing Committees on Animals approved all procedures described according to standards as outlined in The Guide for the Care and Use of Laboratory Animals (UC-IACUC#21-06-01-01). The Institutional Review Board of the University of Cincinnati approved all human relevant studies (UC-IRB#2020-0097).

Author contributions

YX and JJY conceived and designed the study. CL, EYZ conducted experiments and acquired data. AGZ performed quantification of immunoblotting and immunohistochemical staining. TO performed immunoblotting analysis for revision. LP performed TUNEL staining in mouse tissues. RJ supervised statistical analysis. XZ, RH, and KDRS performed lipidomic analysis. KAWB performed quality control and selection of LAM tissues for scRNA-seq. MMM and MK analyzed and interpreted immunohistochemical staining with ASAH1 and DEGS1 in renal angiomyolipomas and normal kidney tissues. EF, DL conducted mouse MRI and data analysis. SZ, MG and YX analyzed scRNA-seq data. EJK, NG, KAWB and FXM assisted with specimen acquisition, data interpretation and clinical context. AA, UM and EYZ analyzed data. AA, EPS, YX and JJY wrote the manuscript. All authors reviewed the final version of the manuscript. AA, CL and EYZ contributed equally and have the right to list their name first in their CV and should be considered co-first authors. The order of co-first authors was determined based on intellectual contribution and volume of work.

Acknowledgments

Funding: Yan Xu and Jane J. Yu are LAM Foundation established investigators. Minzhe Guo is a LAM Foundation early-stage investigator. This study is supported by The LAM Foundation (LAM0138E01-19 and LAM0155S01-22 to YX; LAM0150C01-22 to MG; LAM0131PB07-18 to FXM; LAM0141E01-20 and LAM0133PB07-18 to JJY); National Heart Lung and Blood Institute grants (R01HL153045 to YX and JJY, R01HL138481 to JJY, R01HL160972 to JJY and MK, U01HL148856 to YX); Department of Defense Exploratory Idea Development Award (W81XWH-1910474 to JJY); Department of Defense Idea Development Award (W81XWH-2010736 to JJY); Tuberous Sclerosis Alliance Award (TSA-BSR-03-18 to JJY); CCTST-JIT Award (2UL1TR001425-05A1 to JJY).

We thank The LAM Foundation and the National Diseases Research Interchange, and the Cincinnati Children's Foundation Pathology Research Core for assistance with tissue collection, processing, and

preservation. The LAM Foundation funded the scRNA-seq project. We are grateful for Dr. C. Walker (Baylor College of Medicine) for providing ELT3 cells, and Dr. E.P. Henske (Brigham and Women's Hospital) for providing LAM patient-derived 621-101 and 621-103 cells. We thank Cincinnati Life Center for providing normal lung specimens. We thank the Van Andel Research Institute Biorepository for breeding *Tsc2^{+/-}* A/J mice and the TS Alliance's TSC Preclinical Consortium for providing *Tsc2^{+/-}* A/J mice. We gratefully acknowledge TSC/LAM patients and healthy volunteers for their valuable contribution to this study. Pathway illustrations and graphical abstract were created with BioRender.com.

References

1. Crino PB, Nathanson KL, and Henske EP. The tuberous sclerosis complex. *The New England journal of medicine*. 2006;355(13):1345-56.
2. Henske EP, Jozwiak S, Kingswood JC, Sampson JR, and Thiele EA. Tuberous sclerosis complex. *Nature reviews Disease primers*. 2016;2:16035.
3. Neuman NA, and Henske EP. Non-canonical functions of the tuberous sclerosis complex-Rheb signalling axis. *EMBO molecular medicine*. 2011;3(4):189-200.
4. McCormack FX, and Gupta N. Sporadic lymphangiomyomatosis: Clinical presentation and diagnostic evaluation. <https://www.uptodate.com/contents/sporadic-lymphangiomyomatosis-clinical-presentation-and-diagnostic-evaluation#H4123787339>.
5. Cudzilo CJ, Szczesniak RD, Brody AS, Rattan MS, Krueger DA, Bissler JJ, et al. Lymphangiomyomatosis screening in women with tuberous sclerosis. *Chest*. 2013;144(2):578-85.
6. Kristof AS, Zhi Li P, Major P, and Landry JS. Lymphangiomyomatosis and Tuberous Sclerosis Complex in Quebec: Prevalence and Health-care Utilization. *Chest*. 2015;148(2):444-9.
7. Adriaensen ME, Schaefer-Prokop CM, Duyndam DA, Zonnenberg BA, and Prokop M. Radiological evidence of lymphangiomyomatosis in female and male patients with tuberous sclerosis complex. *Clin Radiol*. 2011;66(7):625-8.
8. Ryu JH, Sykes AM, Lee AS, and Burger CD. Cystic lung disease is not uncommon in men with tuberous sclerosis complex. *Respir Med*. 2012;106(11):1586-90.
9. Carsillo T, Astrinidis A, and Henske EP. Mutations in the tuberous sclerosis complex gene TSC2 are a cause of sporadic pulmonary lymphangiomyomatosis. *Proc Natl Acad Sci U S A*. 2000;97(11):6085-90.

10. Giannikou K, Malinowska IA, Pugh TJ, Yan R, Tseng YY, Oh C, et al. Whole Exome Sequencing Identifies TSC1/TSC2 Biallelic Loss as the Primary and Sufficient Driver Event for Renal Angiomyolipoma Development. *PLoS Genet.* 2016;12(8):e1006242.
11. Strizheva GD, Carsillo T, Kruger WD, Sullivan EJ, Ryu JH, and Henske EP. The spectrum of mutations in TSC1 and TSC2 in women with tuberous sclerosis and lymphangiomyomatosis. *Am J Respir Crit Care Med.* 2001;163(1):253-8.
12. Castro AF, Rebhun JF, Clark GJ, and Quilliam LA. Rheb binds tuberous sclerosis complex 2 (TSC2) and promotes S6 kinase activation in a rapamycin- and farnesylation-dependent manner. *J Biol Chem.* 2003;278(35):32493-6.
13. Duvel K, Yecies JL, Menon S, Raman P, Lipovsky AI, Souza AL, et al. Activation of a metabolic gene regulatory network downstream of mTOR complex 1. *Mol Cell.* 2010;39(2):171-83.
14. Inoki K, Li Y, Xu T, and Guan KL. Rheb GTPase is a direct target of TSC2 GAP activity and regulates mTOR signaling. *Genes Dev.* 2003;17(15):1829-34.
15. Zoncu R, Efeyan A, and Sabatini DM. mTOR: from growth signal integration to cancer, diabetes and ageing. *Nat Rev Mol Cell Biol.* 2011;12(1):21-35.
16. Hay N, and Sonenberg N. Upstream and downstream of mTOR. *Genes Dev.* 2004;18(16):1926-45.
17. Menon S, and Manning BD. Common corruption of the mTOR signaling network in human tumors. *Oncogene.* 2008;27 Suppl 2:S43-51.
18. Schmelzle T, and Hall MN. TOR, a central controller of cell growth. *Cell.* 2000;103(2):253-62.
19. Sarbassov DD, Ali SM, Kim DH, Guertin DA, Latek RR, Erdjument-Bromage H, et al. Rictor, a novel binding partner of mTOR, defines a rapamycin-insensitive and raptor-independent pathway that regulates the cytoskeleton. *Current biology : CB.* 2004;14(14):1296-302.
20. El-Hashemite N, Walker V, Zhang H, and Kwiatkowski DJ. Loss of Tsc1 or Tsc2 induces vascular endothelial growth factor production through mammalian target of rapamycin. *Cancer Res.* 2003;63(17):5173-7.

21. Karbowniczek M, Zitserman D, Khabibullin D, Hartman T, Yu J, Morrison T, et al. The evolutionarily conserved TSC/Rheb pathway activates Notch in tuberous sclerosis complex and *Drosophila* external sensory organ development. *J Clin Invest*. 2010;120(1):93-102.
22. Kenerson HL, Aicher LD, True LD, and Yeung RS. Activated mammalian target of rapamycin pathway in the pathogenesis of tuberous sclerosis complex renal tumors. *Cancer Res*. 2002;62(20):5645-50.
23. Lee L, Sudentas P, Donohue B, Asrican K, Worku A, Walker V, et al. Efficacy of a rapamycin analog (CCI-779) and IFN-gamma in tuberous sclerosis mouse models. *Genes Chromosomes Cancer*. 2005;42(3):213-27.
24. Parkhitko A, Myachina F, Morrison TA, Hindi KM, Auricchio N, Karbowniczek M, et al. Tumorigenesis in tuberous sclerosis complex is autophagy and p62/sequestosome 1 (SQSTM1)-dependent. *Proc Natl Acad Sci U S A*. 2011;108(30):12455-60.
25. Yu JJ, Robb VA, Morrison TA, Ariazi EA, Karbowniczek M, Astrinidis A, et al. Estrogen promotes the survival and pulmonary metastasis of tuberin-null cells. *Proc Natl Acad Sci U S A*. 2009;106(8):2635-40.
26. Bissler JJ, McCormack FX, Young LR, Elwing JM, Chuck G, Leonard JM, et al. Sirolimus for angiomyolipoma in tuberous sclerosis complex or lymphangiomyomatosis. *The New England journal of medicine*. 2008;358(2):140-51.
27. Bissler JJ, Kingswood JC, Radzikowska E, Zonnenberg BA, Frost M, Belousova E, et al. Everolimus for angiomyolipoma associated with tuberous sclerosis complex or sporadic lymphangiomyomatosis (EXIST-2): a multicentre, randomised, double-blind, placebo-controlled trial. *Lancet*. 2013;381(9869):817-24.
28. McCormack FX, Inoue Y, Moss J, Singer LG, Strange C, Nakata K, et al. Efficacy and safety of sirolimus in lymphangiomyomatosis. *The New England journal of medicine*. 2011;364(17):1595-606.

29. Franz DN, Belousova E, Sparagana S, Bebin EM, Frost M, Kuperman R, et al. Efficacy and safety of everolimus for subependymal giant cell astrocytomas associated with tuberous sclerosis complex (EXIST-1): a multicentre, randomised, placebo-controlled phase 3 trial. *Lancet*. 2013;381(9861):125-32.
30. Taveira-DaSilva AM, Hathaway O, Stylianou M, and Moss J. Changes in lung function and chylous effusions in patients with lymphangiomyomatosis treated with sirolimus. *Ann Intern Med*. 2011;154(12):797-805, W-292-3.
31. Davies DM, de Vries PJ, Johnson SR, McCartney DL, Cox JA, Serra AL, et al. Sirolimus therapy for angiomyolipoma in tuberous sclerosis and sporadic lymphangiomyomatosis: a phase 2 trial. *Clin Cancer Res*. 2011;17(12):4071-81.
32. Kwiatkowski DJ. Animal models of lymphangiomyomatosis (LAM) and tuberous sclerosis complex (TSC). *Lymphatic research and biology*. 2010;8(1):51-7.
33. Yu J, and Henske EP. mTOR activation, lymphangiogenesis, and estrogen-mediated cell survival: the "perfect storm" of pro-metastatic factors in LAM pathogenesis. *Lymphatic research and biology*. 2010;8(1):43-9.
34. Franz DN, Leonard J, Tudor C, Chuck G, Care M, Sethuraman G, et al. Rapamycin causes regression of astrocytomas in tuberous sclerosis complex. *Annals of neurology*. 2006;59(3):490-8.
35. Li C, Lee PS, Sun Y, Gu X, Zhang E, Guo Y, et al. Estradiol and mTORC2 cooperate to enhance prostaglandin biosynthesis and tumorigenesis in TSC2-deficient LAM cells. *The Journal of experimental medicine*. 2014;211(1):15-28.
36. Li C, Liu X, Liu Y, Zhang E, Medepalli K, Masuda K, et al. Tuberin Regulates Prostaglandin Receptor-mediated Viability, via Rheb, in mTORC1-hyperactive Cells. *Mol Cancer Res*. 2017.
37. Li C, Zhang E, Sun Y, Lee PS, Zhan Y, Guo Y, et al. Rapamycin-insensitive up-regulation of adipocyte phospholipase A2 in tuberous sclerosis and lymphangiomyomatosis. *PLOS ONE*. 2014;(In Press).

38. Priolo C, Ricoult SJ, Khabibullin D, Filippakis H, Yu J, Manning BD, et al. Tuberous sclerosis complex 2 loss increases lysophosphatidylcholine synthesis in lymphangiomyomatosis. *Am J Respir Cell Mol Biol.* 2015;53(1):33-41.
39. Wang D, and Dubois RN. Eicosanoids and cancer. *Nature reviews Cancer.* 2010;10(3):181-93.
40. Wang MT, Honn KV, and Nie D. Cyclooxygenases, prostanoids, and tumor progression. *Cancer metastasis reviews.* 2007;26(3-4):525-34.
41. De Keijzer S, Meddens MB, Torensma R, and Cambi A. The multiple faces of prostaglandin E2 G-protein coupled receptor signaling during the dendritic cell life cycle. *Int J Mol Sci.* 2013;14(4):6542-55.
42. Lahiri S, and Futerman AH. The metabolism and function of sphingolipids and glycosphingolipids. *Cell Mol Life Sci.* 2007;64(17):2270-84.
43. Ogretmen B. Sphingolipid metabolism in cancer signalling and therapy. *Nature reviews Cancer.* 2018;18(1):33-50.
44. Ghering AB, and Davidson WS. Ceramide structural features required to stimulate ABCA1-mediated cholesterol efflux to apolipoprotein A-I. *Journal of lipid research.* 2006;47(12):2781-8.
45. Witting SR, Maiorano JN, and Davidson WS. Ceramide enhances cholesterol efflux to apolipoprotein A-I by increasing the cell surface presence of ATP-binding cassette transporter A1. *J Biol Chem.* 2003;278(41):40121-7.
46. Ogretmen B, and Hannun YA. Biologically active sphingolipids in cancer pathogenesis and treatment. *Nature reviews Cancer.* 2004;4(8):604-16.
47. Realini N, Solorzano C, Pagliuca C, Pizzirani D, Armirotti A, Luciani R, et al. Discovery of highly potent acid ceramidase inhibitors with in vitro tumor chemosensitizing activity. *Sci Rep.* 2013;3:1035.
48. Nakamura T, Ohno M, Tabuchi Y, Kamigaki T, Fujii H, Yamagishi H, et al. Optimal duration of oral adjuvant chemotherapy with Carmofur in the colorectal cancer patients: the Kansai Carmofur Study Group trial III. *Int J Oncol.* 2001;19(2):291-8.

49. Doan NB, Alhajala H, Al-Gizawiy MM, Mueller WM, Rand SD, Connelly JM, et al. Acid ceramidase and its inhibitors: a de novo drug target and a new class of drugs for killing glioblastoma cancer stem cells with high efficiency. *Oncotarget*. 2017;8(68):112662-74.
50. Islam MM, and Mirza SP. Versatile use of Carmofur: A comprehensive review of its chemistry and pharmacology. *Drug Dev Res*. 2022;83(7):1505-18.
51. Lee PS, Tsang SW, Moses MA, Traves-Gibson Z, Hsiao LL, Jensen R, et al. Rapamycin-insensitive up-regulation of MMP2 and other genes in tuberous sclerosis complex 2-deficient lymphangiomyomatosis-like cells. *Am J Respir Cell Mol Biol*. 2010;42(2):227-34.
52. Guo M, Yu JJ, Perl AK, Wikenheiser-Brokamp KA, Riccetti M, Zhang EY, et al. Single-Cell Transcriptomic Analysis Identifies a Unique Pulmonary Lymphangiomyomatosis Cell. *Am J Respir Crit Care Med*. 2020;202(10):1373-87.
53. Karbowniczek M, Yu J, and Henske EP. Renal angiomyolipomas from patients with sporadic lymphangiomyomatosis contain both neoplastic and non-neoplastic vascular structures. *Am J Pathol*. 2003;162(2):491-500.
54. Lucki N, and Sewer MB. The cAMP-responsive element binding protein (CREB) regulates the expression of acid ceramidase (ASAH1) in H295R human adrenocortical cells. *Biochim Biophys Acta*. 2009;1791(8):706-13.
55. Boyle SC, Liu Z, and Kopan R. Notch signaling is required for the formation of mesangial cells from a stromal mesenchyme precursor during kidney development. *Development*. 2014;141(2):346-54.
56. Xie J, Ponuwei GA, Moore CE, Willars GB, Tee AR, and Herbert TP. cAMP inhibits mammalian target of rapamycin complex-1 and -2 (mTORC1 and 2) by promoting complex dissociation and inhibiting mTOR kinase activity. *Cell Signal*. 2011;23(12):1927-35.
57. Barlow CA, Barrett TF, Shukla A, Mossman BT, and Lounsbury KM. Asbestos-mediated CREB phosphorylation is regulated by protein kinase A and extracellular signal-regulated kinases 1/2. *Am J Physiol Lung Cell Mol Physiol*. 2007;292(6):L1361-9.

58. Pizzirani D, Bach A, Realini N, Armirotti A, Mengatto L, Bauer I, et al. Benzoxazolone carboxamides: potent and systemically active inhibitors of intracellular acid ceramidase. *Angew Chem Int Ed Engl.* 2015;54(2):485-9.
59. Ito K, Yamaguchi A, Miura K, Kato T, Baba S, Matsumoto S, et al. Oral adjuvant chemotherapy with capecitabine (HCFU) for colorectal cancer: five-year follow-up. Tokai HCFU Study Group--third study on colorectal cancer. *J Surg Oncol.* 1996;63(2):107-11.
60. Pollizzi K, Malinowska-Kolodziej I, Stumm M, Lane H, and Kwiatkowski D. Equivalent benefit of mTORC1 blockade and combined PI3K-mTOR blockade in a mouse model of tuberous sclerosis. *Molecular cancer.* 2009;8:38.
61. Koch A, Pfeilschifter J, and Huwiler A. Sphingosine 1-phosphate in renal diseases. *Cell Physiol Biochem.* 2013;31(6):745-60.
62. Choo AY, Kim SG, Vander Heiden MG, Mahoney SJ, Vu H, Yoon SO, et al. Glucose addiction of TSC null cells is caused by failed mTORC1-dependent balancing of metabolic demand with supply. *Mol Cell.* 2010;38(4):487-99.
63. Huang J, Dibble CC, Matsuzaki M, and Manning BD. The TSC1-TSC2 complex is required for proper activation of mTOR complex 2. *Mol Cell Biol.* 2008;28(12):4104-15.
64. Karbowiczek M, Cash T, Cheung M, Robertson GP, Astrinidis A, and Henske EP. Regulation of B-Raf kinase activity by tuberin and Rheb is mammalian target of rapamycin (mTOR)-independent. *J Biol Chem.* 2004;279(29):29930-7.
65. Karbowiczek M, Robertson GP, and Henske EP. Rheb inhibits C-raf activity and B-raf/C-raf heterodimerization. *J Biol Chem.* 2006;281(35):25447-56.
66. Hartman TR, Liu D, Zilfou JT, Robb V, Morrison T, Watnick T, et al. The tuberous sclerosis proteins regulate formation of the primary cilium via a rapamycin-insensitive and polycystin 1-independent pathway. *Human molecular genetics.* 2009;18(1):151-63.
67. Guri Y, Colombi M, Dazert E, Hindupur SK, Roszik J, Moes S, et al. mTORC2 Promotes Tumorigenesis via Lipid Synthesis. *Cancer Cell.* 2017;32(6):807-23 e12.

68. Gu X, Yu JJ, Ilter D, Blenis N, Henske EP, and Blenis J. Integration of mTOR and estrogen-ERK2 signaling in lymphangiomyomatosis pathogenesis. *Proc Natl Acad Sci U S A*. 2013.
69. Sun Y, Zhang E, Lao T, Pereira AM, Li C, Xiong L, et al. Progesterone and estradiol synergistically promote the lung metastasis of tuberin-deficient cells in a preclinical model of lymphangiomyomatosis. *Horm Cancer*. 2014;5(5):284-98.
70. Sun Y, Gu X, Zhang E, Park MA, Pereira AM, Wang S, et al. Estradiol promotes pentose phosphate pathway addiction and cell survival via reactivation of Akt in mTORC1 hyperactive cells. *Cell Death Dis*. 2014;5:e1231.
71. Finlay GA, York B, Karas RH, Fanburg BL, Zhang H, Kwiatkowski DJ, et al. Estrogen-induced smooth muscle cell growth is regulated by tuberin and associated with altered activation of platelet-derived growth factor receptor-beta and ERK-1/2. *J Biol Chem*. 2004;279(22):23114-22.
72. Guenther GG, Liu G, Ramirez MU, McMonigle RJ, Kim SM, McCracken AN, et al. Loss of TSC2 confers resistance to ceramide and nutrient deprivation. *Oncogene*. 2014;33(14):1776-87.
73. Chen J, Bardes EE, Aronow BJ, and Jegga AG. ToppGene Suite for gene list enrichment analysis and candidate gene prioritization. *Nucleic Acids Res*. 2009;37(Web Server issue):W305-11.
74. Howe SR, Gottardis MM, Everitt JI, Goldsworthy TL, Wolf DC, and Walker C. Rodent model of reproductive tract leiomyomata. Establishment and characterization of tumor-derived cell lines. *Am J Pathol*. 1995;146(6):1568-79.
75. Howe SR, Gottardis MM, Everitt JI, and Walker C. Estrogen stimulation and tamoxifen inhibition of leiomyoma cell growth in vitro and in vivo. *Endocrinology*. 1995;136(11):4996-5003.
76. Hong F, Larrea MD, Doughty C, Kwiatkowski DJ, Squillace R, and Slingerland JM. mTOR-raptor binds and activates SGK1 to regulate p27 phosphorylation. *Mol Cell*. 2008;30(6):701-11.
77. Hammad SM, Pierce JS, Soodavar F, Smith KJ, Al Gadban MM, Rembiesa B, et al. Blood sphingolipidomics in healthy humans: impact of sample collection methodology. *Journal of lipid research*. 2010;51(10):3074-87.

78. Chou TC, and Martin N. CompuSyn for Drug Combinations: PC Software and User's Guide: A Computer Program for Quantitation of Synergism and Antagonism in Drug Combinations, and the Determination of IC50 and ED50 and LD50 Values. www.combosyn.com.
79. Onda H, Lueck A, Marks PW, Warren HB, and Kwiatkowski DJ. Tsc2(+/-) mice develop tumors in multiple sites that express gelsolin and are influenced by genetic background. *J Clin Invest*. 1999;104(6):687-95.
80. Woodrum C, Nabil A, and Dabora SL. Comparison of three rapamycin dosing schedules in A/J Tsc2+/- mice and improved survival with angiogenesis inhibitor or asparaginase treatment in mice with subcutaneous tuberous sclerosis related tumors. *Journal of translational medicine*. 2010;8:14.
81. Kalogerou M, Zhang Y, Yang J, Garrahan N, Paisey S, Tokarczuk P, et al. T2 weighted MRI for assessing renal lesions in transgenic mouse models of tuberous sclerosis. *Eur J Radiol*. 2012;81(9):2069-74.

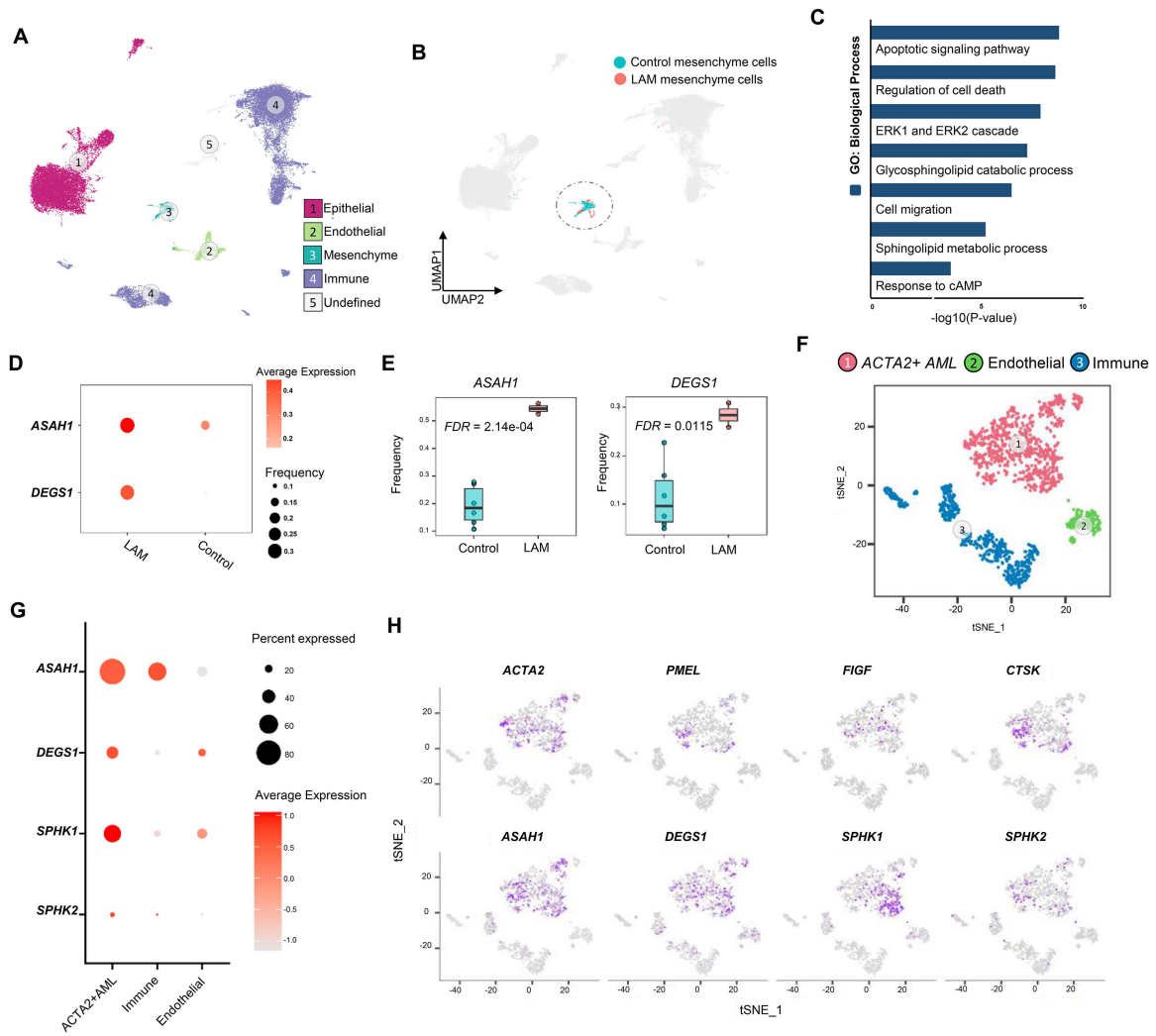


Figure 1. Single-cell RNA sequencing (scRNA-seq) analysis identified Sphingolipids pathways and related genes induced in LAM mesenchymal cells and renal angiomyolipoma (AML) ACTA2+ AML cells. **(A)** Integration of 54,511 cells from two LAM lung samples and six control lung samples. Cells are visualized using Uniform Manifold Approximation and Projection (UMAP). Cells are colored by major lineages. **(B)** 736 mesenchymal cells from control samples and 190 mesenchyme cells from LAM lung sample are integrated and extracted for direct comparison. **(C)** Functional enrichment analysis of genes induced in LAM mesenchymal cells vs. control mesenchymal cells. **(D)** Dot plots showing the increasing expression and frequency of *ASAH1* and *DEGS1* in LAM vs control. Node size represents gene expression frequency. Node color represents the scaled average expression. **(E)** Box plots showing the expression frequency of representative sphingolipid biosynthesis pathway genes in control mesenchymal cells and LAM mesenchymal cells. **(F)** Visualization of 1,583 cells from lesions of renal angiomyolipoma (AML) tumor cells. Cells are visualized using t-Distributed Stochastic Neighbor Embedding (tSNE). Cells are colored by condition. AML lesions consist of three major cell types: ACTA2+ AML cells (largest cluster), immune cells and endothelial cells. AML scRNAseq data was downloaded from GEO, accession number GSM4035469; and cell type annotation is done based on the previous study (52). **(G)** Dot plot showing selected sphingolipid biosynthesis pathway genes expression comparison across the three AML cell populations. Node size represents gene expression frequency. Node color represents the scaled average expression. **(H)** Feature plots of known LAM and AML markers (*ACTA2*, *PMEL*, *FIGF*, and *CTSK*) and sphingolipid pathway genes (*ASAH1*, *DEGS1*, *SPHK1*, and *SPHK2*) in AML cells.

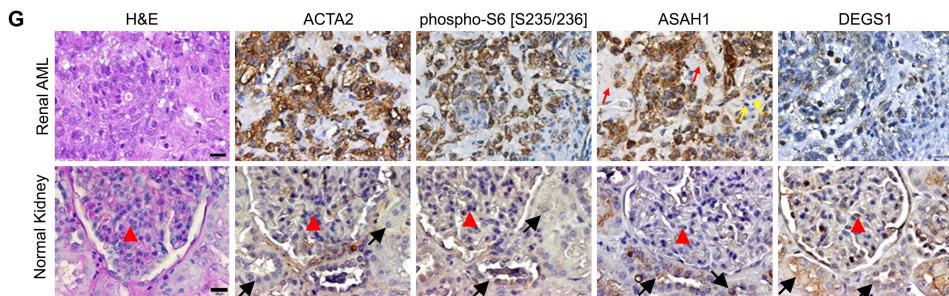
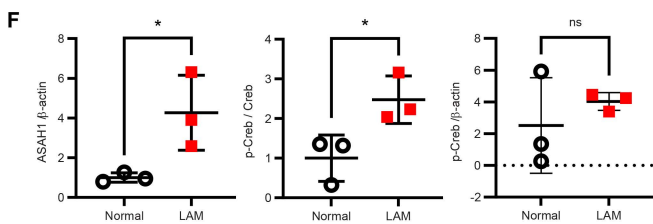
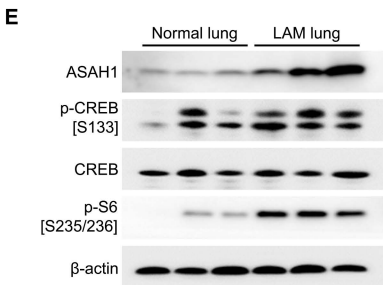
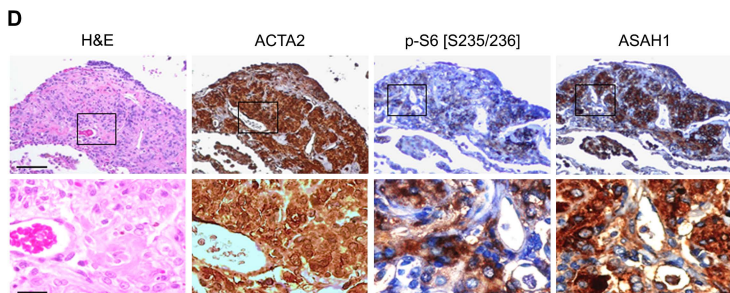
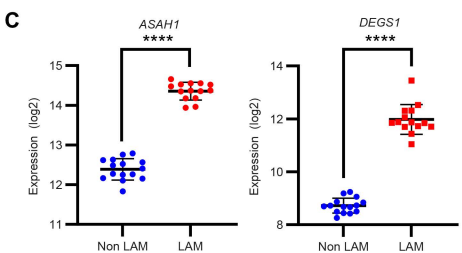
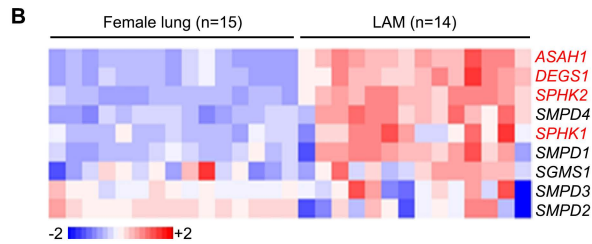
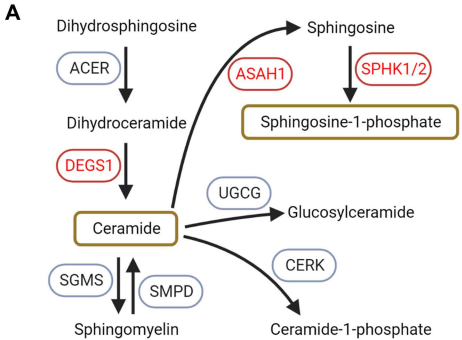


Figure 2. Expression of DEGS1 and ASAH1 is evident in pulmonary LAM lesions. (A)

Sphingolipid biosynthesis pathway shows genes with upregulated expression in TSC2-null cells (in red). **(B)** Heatmap of sphingolipid metabolism genes expression in female non-LAM female lungs (n=15 subjects) and laser capture microdissected LAM lesion cells (n=14 subjects). **(C)** *ASAH1* expression in LAM cells, compared to control female non-LAM lungs. **** P < 0.0001, Mann-Whitney test. **(D)** Immunohistochemistry of hematoxylin and eosin (H&E), smooth muscle actin (ACTA2), phospho-S6 [Ser235/236], and ASAH1 in LAM lung tissues. Representative images of 3 cases are shown. Scales are 100 and 20 μm for the top and bottom rows, respectively. **(E)** Immunoblotting of ASAH1 and transcription factor CREB in LAM and control lungs (n=3). **(F)** Densitometry of ASAH1 and phospho-CREB (n=3). * P < 0.05, unpaired t test. **(G)** H&E, ACTA2, phospho-S6 [Ser235/236], ASAH1, and DEGS1 in renal AML and normal kidney. Representative images of 3 cases are shown. Scales are 20 μm .

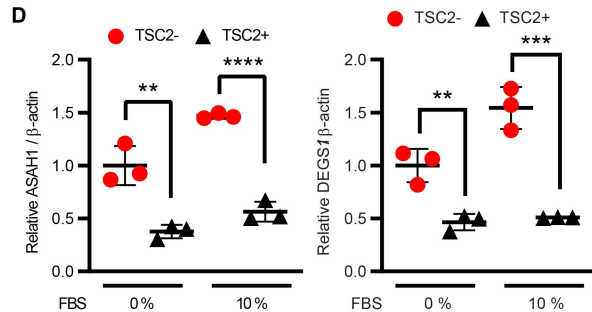
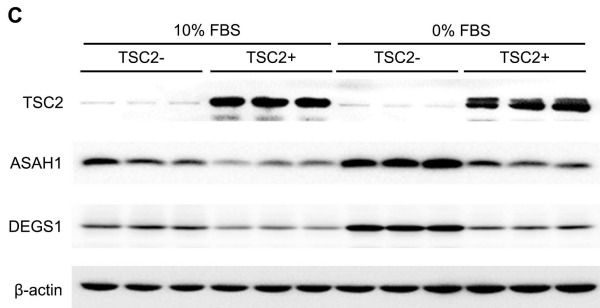
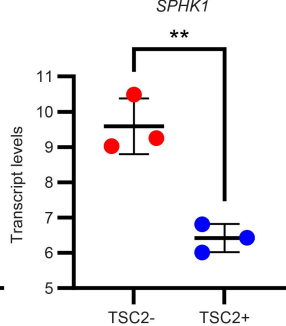
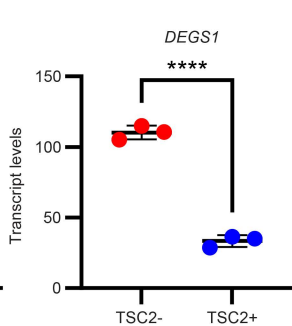
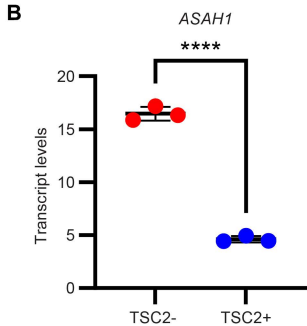
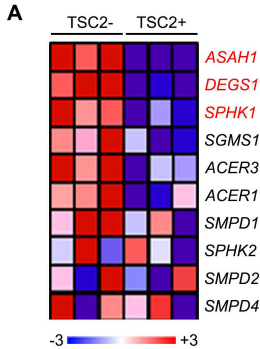


Figure 3. Upregulation of acid ceramidase (ASAH1) and dihydroceramide desaturase (DEGS1) expression in TSC2-null LAM-derived cells. (A) Heatmap of the expression of sphingolipid biosynthesis pathway genes in TSC2-null (TSC2-) 621-102 and TSC2-addback (TSC2+) 621-103 cells. The scale indicates the fold change of genes from blue (min) to red (max) (-3 to +3). (B) Transcript levels of *ASAH1*, *DEGS1*, and *SPHK1* in TSC2-null patient-derived 621-102 and 621-103 cells. (C) The protein levels of TSC2, DEGS1, and ASAH1 were assessed by immunoblotting. β -actin was used as a loading control. (D) Densitometry of ASAH1 and DEGS1 protein levels normalized to β -actin (n=3/group). (B and D) ** P < 0.01, *** P < 0.001, **** P < 0.0001, unpaired t test.

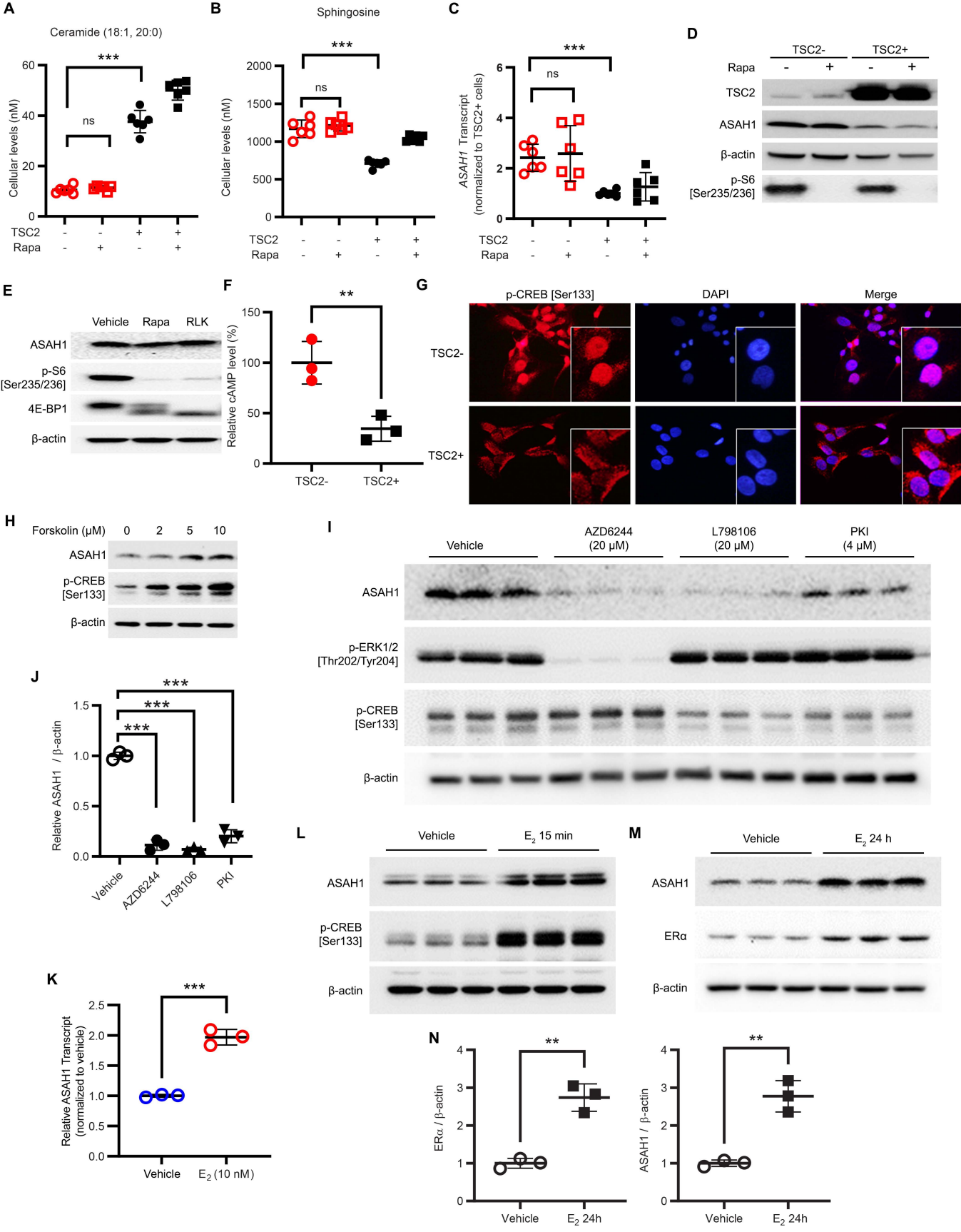


Figure 4. ASAH1 activity and expression are elevated in a sirolimus-insensitive manner in LAM-derived cells. 621-101 (TSC2-) and 621-103 (TSC2+) cells were treated with 20 nM sirolimus (Rapa) for 24 hr. Cellular levels of ceramide (**A**) and sphingosine (**B**) were quantified using LC-MS/MS. (**C**) *ASAH1* transcript levels were quantified by qRT-PCR. (**D** and **E**) LAM patient-derived 621-101 (TSC2-) and 621-103 (TSC2+) cells were treated with mTORC1 inhibitor rapamycin (Rapa) (20 nM) or rapalink-1 (RLK1) (0.1 μ M) for 24 hr. Protein levels of TSC2, ASAH1, phospho-S6 [Ser235/236], and 4E-BP1 were assessed by immunoblotting. β -actin was used as a loading control. (**F**) Cellular levels of cAMP were quantified in 621-101 (TSC2-) and 621-103 (TSC2+) cells (n=3). (**G**) Representative images of confocal microscopy of phospho-CREB are shown. Nuclei were stained with DAPI. (**H** and **I**) 621-101 (TSC2-) cells were treated with cAMP agonist forskolin (2, 5, and 10 μ M), MEK1/2 inhibitor AZD6244 (20 μ M), prostaglandin E2 receptor 3 (EP3) inhibitor L798106 (20 μ M), or protein kinase A inhibitor (PKI) (4 μ M), for 24 hr. Protein levels of ASAH1, phospho-CREB (S133), and phospho-Erk1/2 were assessed by immunoblotting. β -actin was used as a loading control. (**J**) Densitometry of ASAH1 protein levels normalized to β -actin (n=3). (**K-M**) 621-101 (TSC2-) cells were treated with 10 nM E₂ for 15 min or 24 hr. *ASAH1* transcript levels were quantified using qRT-PCR. Immunoblot analyses of phospho-CREB [Ser133], ASAH1, and ER α were performed (n=3/group). β -actin was used as a loading control. (**N**) Densitometry of ER α and ASAH1 protein levels (n=3). (**A-C, F, J, K, N**) ns = not significant, ** P < 0.01, *** P < 0.001, **** P < 0.0001. (**A-C, J**) Unpaired t test with Bonferroni multiple comparison adjustment. (**F, K, N**) Unpaired t test.

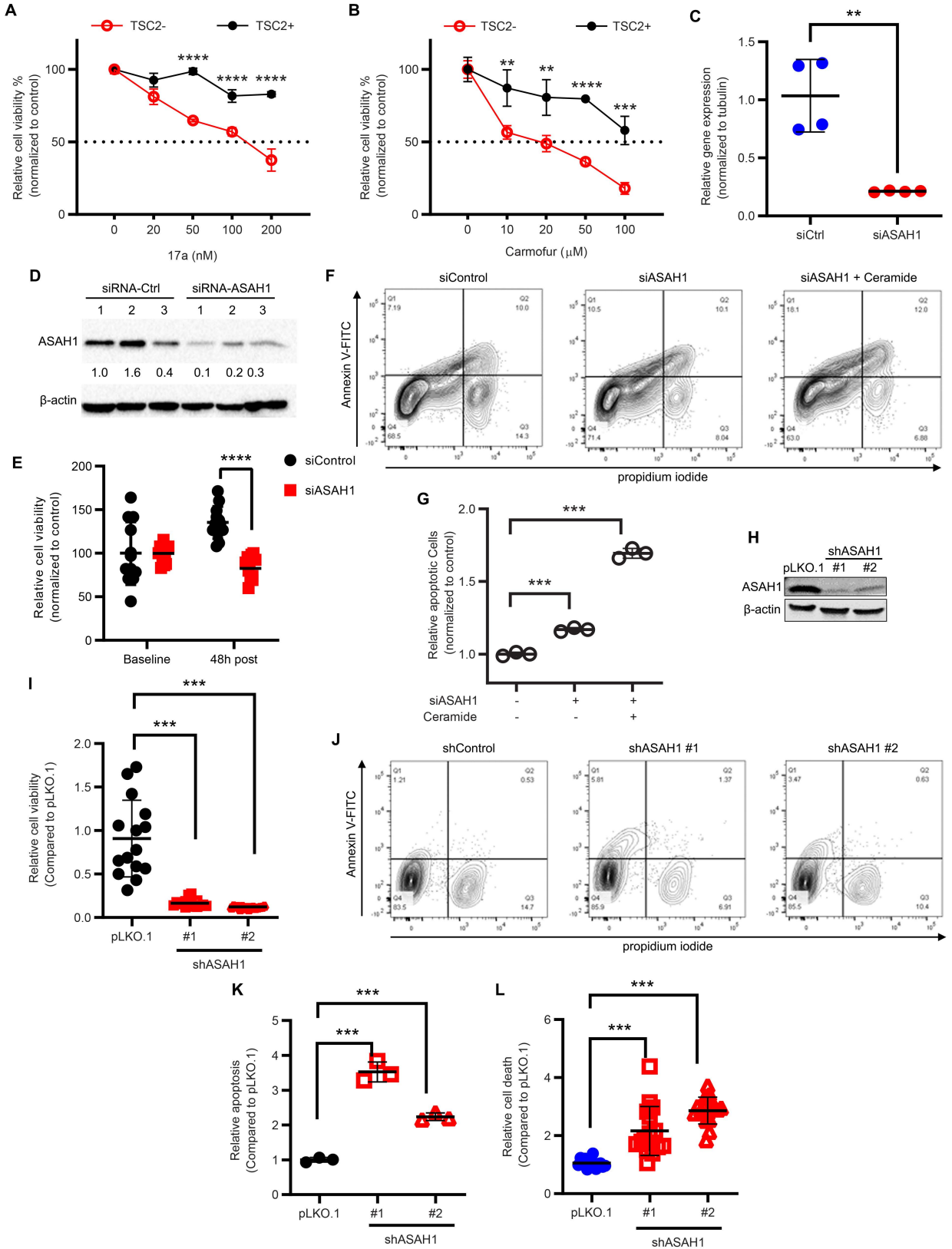


Figure 5. Suppression of ASAH1 decreases the survival of TSC2-null cells in vitro. 621-101 (TSC2-) and 621-103 (TSC2+) cells were treated with an ASAH1 inhibitor 17a (**A**) or carmofur (**B**) with indicated concentrations for 72 hr. Cell viability was measured using MTT assay (n=6/treatment group). Error bars are SEM. (**C**) TSC2-null 621-101 cells were transfected with three independent ASAH1-siRNAs or control-siRNA for 48 hr. siRNA knockdown efficiency was determined by RT-PCR (n=3/group) and (**D**) immunoblotting analysis. Fold change of ASAH1/ β -actin was determined using densitometry analysis. β -actin was used as a loading control. (**E**) Cell viability was assessed 48 hr post siASAH1 RNA transfection in 621-101 cells using MTT assay (n=12/treatment group). (**F**) Cells were treated with ceramide, and then stained with Annexin V: FITC Apoptosis Detection Kit (BD#556547). Cell death was analyzed by flow cytometry (n=3). (**G**) The percentage of apoptotic (Annexin V+) cells was determined (percentage of Annexin V: FITC-positive cells in total cell number). (**H**) 621-101 cells were infected with lentiviruses containing shRNA for vector pLKO.1, or *ASAH1*, and then selected with puromycin for two weeks. shRNA knockdown efficiency was determined by immunoblotting. β -actin was used as a loading control. (**I**) Viability of 621-101 cells transduced with pLKO.1 or *ASAH1* shRNA was measured by MTT assay (n=8-16/treatment group). (**J**) Stable cells were harvested, and then stained with Annexin V: FITC Apoptosis Detection Kit. Cell death was analyzed by flow cytometry (n=3). (**K**) The percentage of apoptotic (Annexin V+) cells was determined (percentage of Annexin V: FITC-positive cells in total cell number). (**L**) Cell death was measured using PI exclusion assay. Relative cell death was compared between pLKO.1 and shRNA-*ASAH1* cells. (**A-C, E, G, I, K, L**) ** P < 0.01, *** P < 0.001, **** P < 0.0001. (**A-C, E**) Unpaired t test. (**G, I, K, L**) Unpaired t test with Bonferroni multiple comparison adjustment.

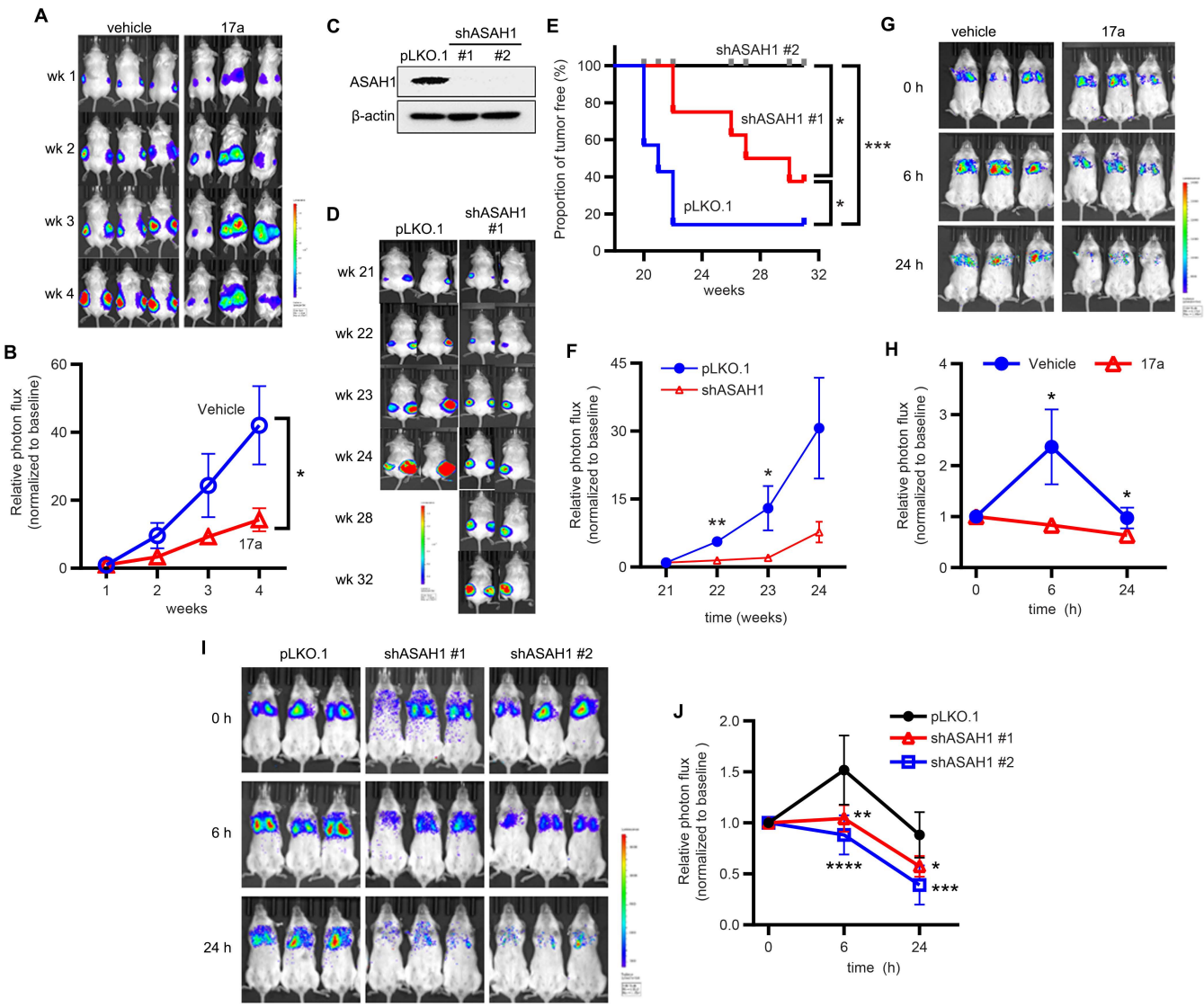


Figure 6. Suppression of *ASAH1* decreases the survival of *TSC2*-null cells in vivo. (A) Female NSG mice were inoculated subcutaneously with 2×10^6 ELT3-luciferase expressing cells. Weekly bioluminescent imaging was performed. Upon ELT3 tumor onset, mice were randomized and treated with vehicle or 17a (10 mg/kg/day, i.p.) for four weeks. (B) Tumor photon flux was quantified and normalized to the baseline measurements (Week 0). Weekly bioluminescent imaging was performed. (C) 621-101 cells expressing luciferase (621L9) were infected with lentivirus of *ASAH1*-shRNA cells or control pLKO.1 empty vector. *ASAH1* knockdown efficiency was determined by immunoblotting. β -actin was used as a loading control. (D) Female NSG mice were subcutaneously inoculated with 2×10^6 621-101-pLKO.1 or 621-101-sh*ASAH1* cells. Tumor formation was detected 21-weeks post cell inoculation. Weekly bioluminescent imaging was performed for up to 32 weeks. (E) Kaplan-Meier percent tumor-free survival curve. (F) Tumor photon flux was quantified and normalized to the baseline measurements (Week 21) (n=3-4/group). (G) Female NSG mice were treated with vehicle or 17a (10 mg/kg/day, i.p.) for two days and then intravenously inoculated with 2×10^5 621L9 cells. Bioluminescent imaging was performed 1-24 hours post-cell inoculation (n=3). (H) Photon flux at the chest region was quantified. (I) Female NSG mice were intravenously inoculated with 2×10^5 621L9-*ASAH1*-shRNA (#1 and #2) cells or control pLKO.1 cells. Bioluminescent imaging was performed 1-24 hours post cell inoculation (n=4-5). (J) Photon flux at the chest region was quantified. (B, E, F, H, J) * P < 0.05, ** P < 0.01, *** P < 0.001, **** P < 0.0001. (B, F, H) Unpaired t test. (E) Log-rank (Mantel-Cox) test. (J) Two-way ANOVA with Tukey's multiple comparisons test.

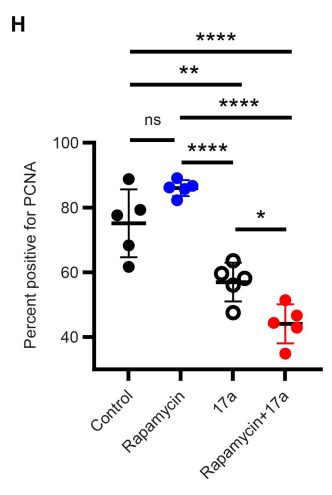
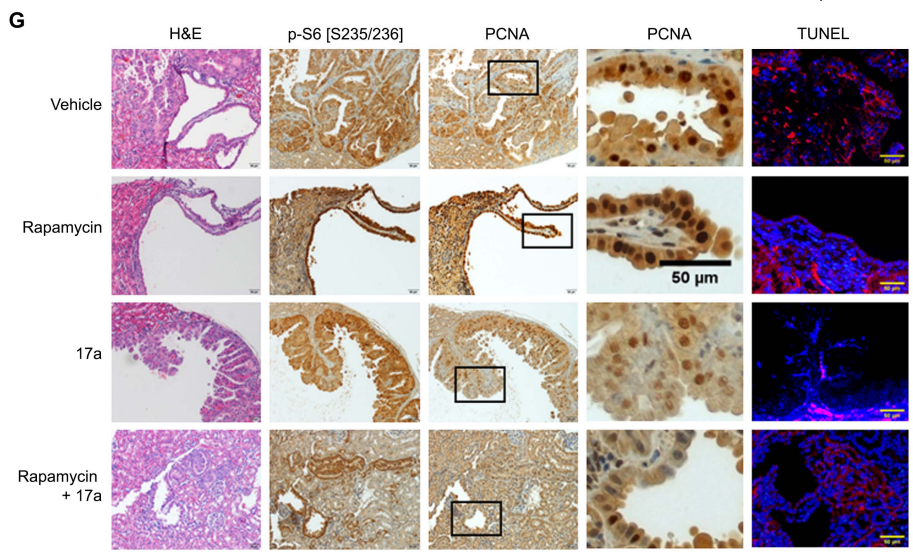
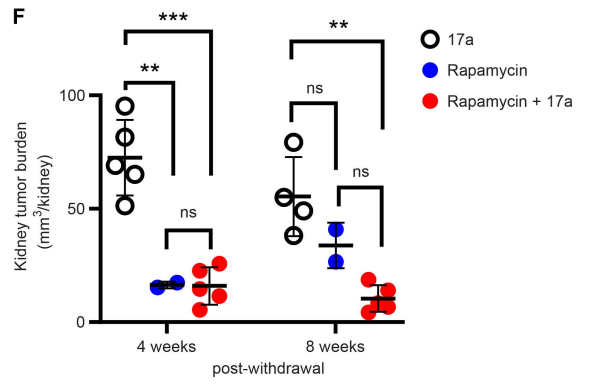
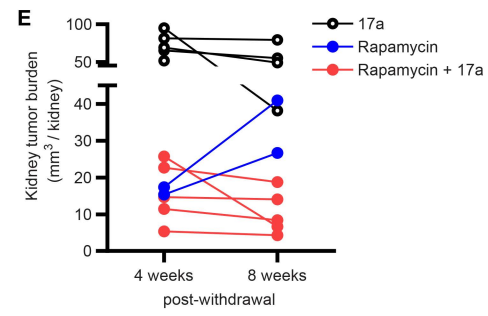
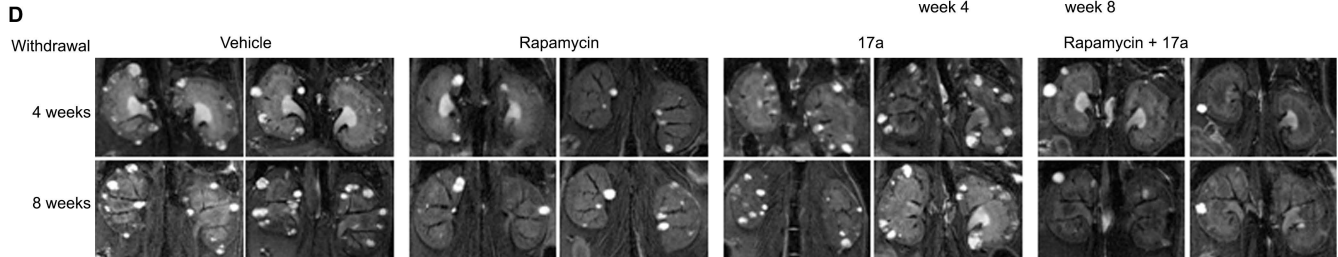
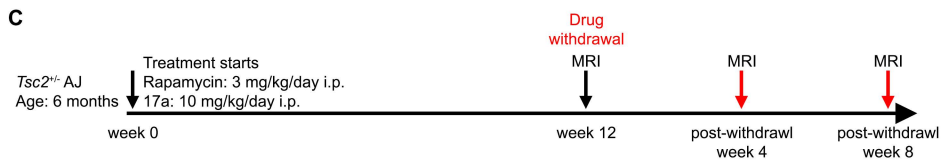
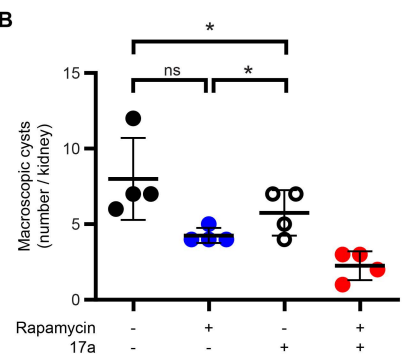
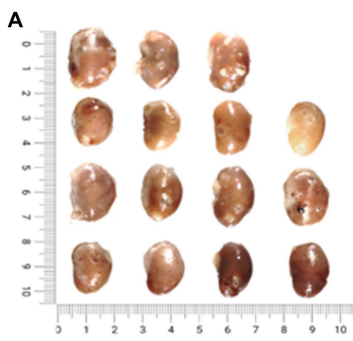


Figure 7. Combination of ASAH1 and mTORC1 inhibition suppresses Tsc2-null tumor growth and tumor regrowth better than rapamycin alone. *Tsc2*^{+/-} AJ mice were given vehicle, rapamycin, 17a, rapamycin and 17a combinatorial treatment for 12 weeks (n=4 mice/group). Macroscopic analysis (**A**) and quantification (**B**) of renal tumor burden under a dissection microscope upon drug withdrawal. (**C**) Tumor rebound study and MRI follow up post-treatment schema. (**D-F**) MRI imaging of *Tsc2*^{+/-} AJ mouse kidneys at 4 and 8 weeks after withdrawal from treatment. ** P<0.01, *** P<0.001 ANOVA and Tukey's multiple comparison test. (**G**) Mouse kidney sections were stained with H&E, phospho-S6 [Ser235/236], PCNA, and TUNEL. Scales are 20 μm. (**H**) Percentages of cells with nuclear immunoreactivity for PCNA were scored from five random fields per section. * P < 0.05, ** P < 0.01, Mann-Whitney test. (**B, F, H**) ns = not significant, ** P < 0.01, *** P < 0.001, **** P < 0.0001. (**B**) Unpaired t test with Bonferroni multiple comparison adjustment. (**F and H**) One-way ANOVA with Tukey's multiple comparisons test.

Table 1. Optimized conditions for quantification of sphingosine and internal standard by ESI-UPLC-MS/MS

Analyte	MRM transitions (m/z)	Ion	Cone voltage (V)	Collision (V)	Retention time (min)
Sphingosine	300.4 -> 282.3	Quantifier	35	10	5.7
	300.4 -> 252.3	Qualifier	35	10	5.7
Sphingosine (d17:1)	286.4 -> 268.4	Quantifier	35	10	5.5
	286.4 -> 238.4	Qualifier	35	10	5.5

Table 2. Optimized conditions for quantification of ceramides and internal standard by ESI-UPLC-MS/MS

Analyte	MRM transitions (m/z)	Dwell (s)	Cone voltage (V)	Collision (V)	Retention time (min)
Ceramide (d18:1/16:0)	520.6 -> 264.3	0.1	35	25	6.7
Ceramide (d18:1/18:0)	548.7 -> 264.3	0.1	35	25	7.3
Ceramide (d18:1/20:0)	576.7 -> 264.4	0.1	35	25	7.9
Ceramide (d18:1/22:0)	604.7 -> 264.4	0.1	35	25	8.6
Ceramide (d18:1/24:0)	632.7 -> 264.4	0.1	35	25	10.0
Ceramide (d18:1/26:0)	660.8 -> 264.4	0.1	35	25	10.2
Ceramide (d18:1/17:0)	534.6 -> 264.3	0.1	35	20	7.0